Cell Reports

Article

Cellular Mg^{2+} decrease causes a distinctive NF-κB-dependent form of cell death

Graphical abstract

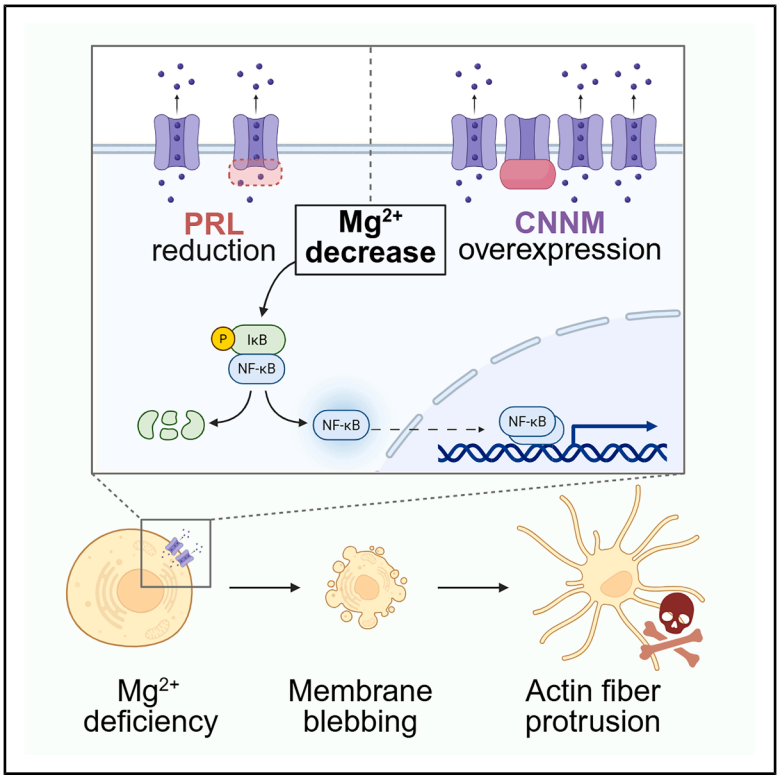

Authors

Koyuki Kawamura, Koya Ono, Eikan Mishima, Osamu Hashizume, Marcus Conrad, Hiroaki Miki, Yosuke Funato

Correspondence

miki.hiroaki.4e@kyoto-u.ac.jp (H.M.), funato.yosuke.3i@kyoto-u.ac.jp (Y.F.)

In brief

Mg^{2+} is crucial for various cellular functions, but the effect of intracellular Mg^{2+} decrease remains obscure. Kawamura et al. show that the decrease triggers massive cell death by activating the NF-κB signal. Furthermore, cell death is distinct from the known types of regulated cell death, which are characterized by actin-driven protrusions.

Highlights

- PRL depletion or CNNM expression induces intracellular Mg^{2+} decrease and massive cell death
- Activation of the NF-κB pathway is crucial for Mg^{2+} decrease-mediated cell death
- Dying cells show distinctive features, marked by actin-driven fiber-like protrusions

Kawamura et al., 2026, Cell Reports *45*, 116964
February 24, 2026
https://doi.org/10.1016/j.celrep.2026.116964

CellPress

Cell Reports

CellPress
OPEN ACCESS

Article

Cellular Mg^{2+} decrease causes a distinctive NF-κB-dependent form of cell death

Koyuki Kawamura,[1] Koya Ono,[2] Eikan Mishima,[2,3] Osamu Hashizume,[1] Marcus Conrad,[2,4] Hiroaki Miki,[1,*] and Yosuke Funato[1,5,*]

[1]Laboratory of Biorecognition Chemistry, Department of Synthetic Chemistry and Biological Chemistry, Graduate School of Engineering, Kyoto University, Katsura, Nishikyo-ku, Kyoto 615-8510, Japan

[2]Institute of Metabolism and Cell Death, Helmholtz Zentrum München, Ingolstädter Landstraße 1, Neuherberg 85764, Germany

[3]Department of Redox Molecular Medicine, Graduate School of Medicine, Tohoku University, 2-1 Seiryo-machi, Aoba-ku, Sendai, Miyagi 980-8575, Japan

[4]Translational Redox Biology, Natural School of Sciences, Technical University of Munich, Garching 85748, Germany

[5]Lead contact

*Correspondence: miki.hiroaki.4e@kyoto-u.ac.jp (H.M.), funato.yosuke.3i@kyoto-u.ac.jp (Y.F.)

https://doi.org/10.1016/j.celrep.2026.116964

SUMMARY

Mg^{2+} is an essential cofactor for numerous enzymes, supporting fundamental cellular processes. The phosphatase of regenerating liver (PRL) protein family, frequently upregulated in cancer, inhibits cyclin M (CNNM) Mg^{2+} efflux transporters. To elucidate the physiological role of PRL in Mg^{2+} homeostasis at the cellular level, we employed combined genetic knockout and knockdown approaches. PRL deletion led to marked reduction of intracellular Mg^{2+} levels and triggered extensive cell death. Transcriptomic analysis revealed activation of the NF-κB pathway, and, accordingly, the genetic deletion of NF-κB p65 subunit abrogated cell death. Similarly, CNNM overexpression triggered intracellular Mg^{2+} decrease, NF-κB activation, and subsequent cell death. Notably, this form of cell death exhibited characteristic morphological features, including actin-driven fiber-like protrusions, distinguishing it from known cell death modalities. Our findings uncover a distinct mode of NF-κB-dependent cell death triggered by intracellular Mg^{2+} decrease.

INTRODUCTION

Magnesium ion (Mg^{2+}) is the most abundant divalent cation in cells, where it predominantly exists in a bound form with cellular molecules, such as ATP, nucleic acids, proteins, and phospholipids. As an essential cofactor for a wide range of enzymatic reactions, Mg^{2+} is indispensable for a myriad of cellular functions, including energy metabolism, nucleic acid synthesis, and genome stability.[1] Intracellular Mg^{2+} levels are tightly regulated (∼17–20 mM) by the coordinated activities of a series of Mg^{2+}-permeable channels and transporters, including transient receptor potential melastatin 6 (TRPM6); TRPM7; magnesium transporter 1; mitochondrial RNA splicing 2 and its prokaryotic ortholog CorA, solute carrier family 41 member A1 (SLC41A1), and MgtE; and cyclin M (CNNM) and CorB/CorC.[2–13] In particular, the CNNM family of proteins plays a pivotal role in extruding Mg^{2+} for maintaining cellular Mg^{2+} homeostasis, as supported by studies showing that CNNM overexpression or its loss profoundly impacts intracellular Mg^{2+} levels.[4,14–22]

Importantly, phosphatase of regenerating liver (PRL) binds and inhibits CNNM-dependent Mg^{2+} efflux, thereby elevating intracellular Mg^{2+}.[14,23] Three *PRL* family genes (*PRL1–3*) are present in mammals, which encode highly homologous proteins possessing a single protein tyrosine phosphatase (PTP) domain and a C-terminal prenylation signal (CAAX) sequence for membrane anchoring[24] (Figure 1A). Although initially identified in liver regeneration,[25] PRLs have been implicated in metastatic progression of colorectal and other cancers.[26] The expression level of PRLs is frequently upregulated in tumor tissues,[27] and previous studies indicated that PRL promotes tumor progression through its interaction with CNNM.[28] For instance, the overexpression of PRLs elevates intracellular Mg^{2+} levels and affects cellular physiology, including increased levels of ATP and reactive oxygen species, altered lysosomal dynamics, and modulation of key signaling pathways such as AMPK, TORC1/2, and EGFR.[14,29–33]

While loss-of-function studies have been performed in both organisms and cell lines, the physiological functions of PRLs remain incompletely defined, especially at the cellular level. Single-gene knockout (KO) mice of *Prl1* or *Prl3* show only subtle phenotypes,[34,35] while *Prl2* KO mice show growth retardation.[36,37] *Prl1*/*Prl2* double KO results in embryonic lethality,[34] suggesting compensatory functions among the PRL family proteins. In addition, *prl-1* mutation in *Drosophila melanogaster* and *Caenorhabditis elegans*, which possess a single orthologous gene of mammalian *PRL* (*prl-1*), did not affect body size and morphology,[32,38] suggesting a complex role for PRL at the organismal level. At the cellular level, earlier studies using KO or knockdown (KD) approaches to target PRLs often failed to achieve complete PRL depletion, leaving residual protein expression with little impact on Mg^{2+} levels or cell proliferation.[39] These results indicate that a more robust suppression of PRL family expression is required to clarify the physiological role of

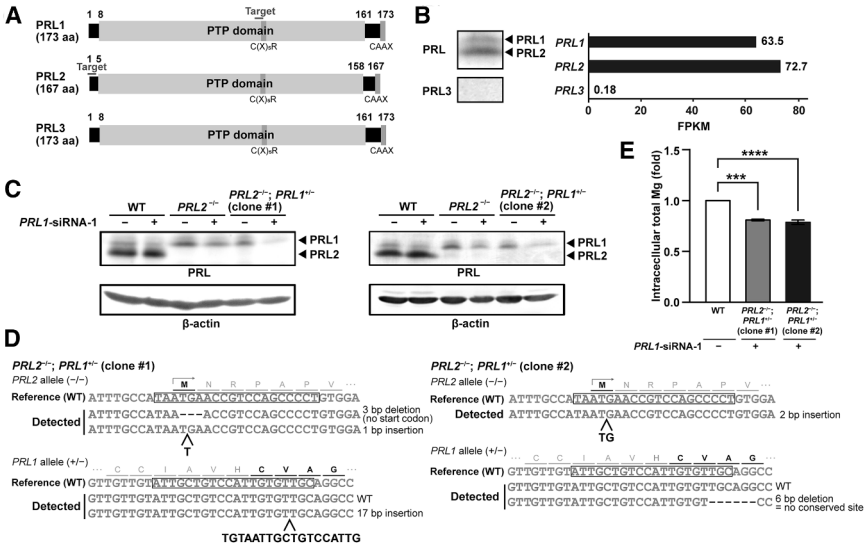

Figure 1. Near-complete suppression of PRL expression in MDCK cells

(A) Domain structure of PRL protein family (Genbank: XP_005627571.1 for canine PRL1, Genbank: XP_038317850.1 for canine PRL2, and Genbank: XP_005628061.1 for canine PRL3). PTP, protein tyrosine phosphatase. Phosphatase motif $[C(X)_5R]$, CAAX sequence, and sgRNA target sites are also indicated.

(B) Left, lysates of MDCK cells were subjected to immunoblotting with the indicated antibodies. Right, RNAs were isolated from MDCK cells and subjected to RNA-seq analysis. mRNA levels are shown as fragments per kilobase of exon per million mapped reads values.

(C) Indicated MDCK-derived cell lines were transfected twice with control siRNA ("−") or *PRL1*-siRNA-1 ("+"), and the lysates (collected 6 h after the second transfection) were subjected to immunoblotting with indicated antibodies.

(D) Genomic sequencing analysis of MDCK-derived cell lines. Detected sequences are shown below the reference WT sequence. Boxed letters, sgRNA target sites. Amino acid sequences of WT PRL2 and PRL1 are also shown, and the first methionine of PRL2 and the phosphatase motif of PRL1 are indicated with black letters.

(E) Indicated MDCK-derived cell lines were transfected twice with control siRNA ("−") or *PRL1*-siRNA-1 ("+"). Total intracellular Mg contents were quantified at 6 h after the second transfection with xylidyl blue (mean ± SEM, $n = 3$ biological replicates). ***$p < 0.01$ and ****$p < 0.0001$ (one-way ANOVA).

See also Figure S1.

the PRL family in maintaining Mg^{2+} homeostasis at the cellular level.

In this study, we succeeded in achieving a near-complete suppression of PRL family expression in Madin-Darby canine kidney (MDCK) cells using a combined KO and KD strategy. This approach led to a profound decrease in intracellular Mg^{2+} levels and triggered a striking form of cell death clearly different from known cell death modalities but dependent on NF-κB signaling. Our findings therefore reveal an unexpected mode of intracellular Mg^{2+}-dependent cell death pathway.

RESULTS

Experimental setup to achieve near-complete deletion of the PRL family

To be able to investigate the physiological role of the PRL family in Mg^{2+} homeostasis, we aimed to robustly delete the PRL family expression in MDCK epithelial cells, which are frequently used in cellular ion transport studies. In mammals, three *PRL* family genes (*PRL1–3*) encode highly homologous proteins, sharing 77%–86% identity among their canine orthologs (Figure 1A). Immunoblotting with an anti-PRL antibody that recognizes all three isoforms[14] revealed a lower band corresponding to PRL2 and an upper band representing PRL1 and/or PRL3 (Figure 1B). Subsequent immunoblotting using a PRL3-specific antibody did not yield a detectable signal, suggesting negligible PRL3 expression. Transcriptomic analysis of MDCK cells confirmed this expression profile: PRL2 showed the highest expression, PRL1 was moderately expressed, and PRL3 expression was negligible. Based on these findings, we targeted *PRL1* and *PRL2* to suppress total PRL activity in MDCK cells.

We first generated *PRL2* KO ($PRL2^{-/-}$) clones by lentiviral delivery of Cas9 and a single guide RNA (sgRNA) targeting *PRL2* (Figure 1A). Successful *PRL2* disruption in two independent cell clones was confirmed (Figures 1C and 1D). $PRL2^{-/-}$ clones exhibited enhanced PRL1 expression, consistent with previous observations in *PRL2* KO or KD models.[39–41] We next attempted to generate *PRL2*/*PRL1* double-KO cells from *PRL2* single-KO cells. However, only heterologous *PRL1* disruption clones ($PRL2^{-/-}$; $PRL1^{+/-}$ cells) were obtained, suggesting that complete *PRL1/2* ablation impairs cell viability. In support of this, *PRL1* single-KO clones could be generated from wild-type (WT) cells using the same sgRNA (Figure S1), implying that *PRL1/2* double KO causes severely impaired proliferation or cell death. To further reduce the remaining PRL1 expression, we transfected the *PRL1*-specific siRNA (*PRL1*-siRNA-1) into $PRL2^{-/-}$; $PRL1^{+/-}$ cells. This combined KO and KD approach (hereafter referred to as *PRL* KO + KD) markedly decreased PRL1 protein levels (Figure 1C). Given that PRLs suppress CNNM-mediated Mg^{2+} efflux,[14] we hypothesized that *PRL* KO + KD would lead to decreased intracellular Mg^{2+}. Indeed, *PRL* KO + KD by introducing *PRL1*-siRNA-1 into either $PRL2^{-/-}$; $PRL1^{+/-}$ #1 or $PRL2^{-/-}$; $PRL1^{+/-}$ #2 cells resulted in a significant decrease in Mg content (Figure 1E), confirming a critical role for PRLs in maintaining intracellular Mg levels.

PRL deletion triggers massive cell death

We found that *PRL* KO + KD cells exhibited a marked increase in detached cells (Figure 2A), suggesting that *PRL* deletion impairs cell proliferation and/or viability. For the subsequent analysis, we reseeded the cells at a low density following the *PRL1* siRNA transfection and performed time-course experiments. In time-lapse imaging, the control cells actively proliferated and reached ~80% confluence within 48 h, while *PRL* KO + KD cells largely failed to proliferate (Figure 2B; Videos S1 and S2). Trypan blue exclusion assays also demonstrated that *PRL* KO + KD cells

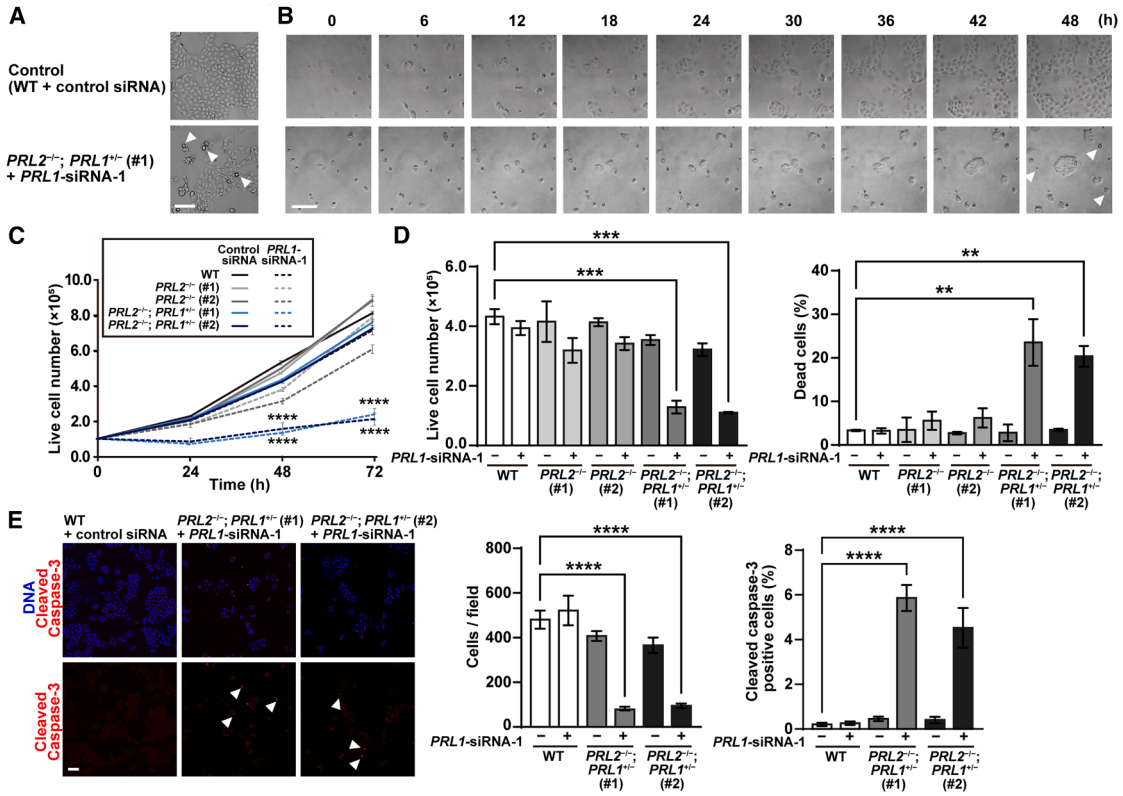

Figure 2. Near-complete suppression of PRL causes cell death

Indicated MDCK-derived cell lines were transfected twice with control siRNA ("−") or *PRL1*-siRNA-1 ("+"). (A) Phase-contrast images at 6 h after the second transfection. Arrowheads: detached cells. (B) From 3 h after reseeding, phase-contrast images were acquired every 1 h for 48 h, and representative images at 6-h intervals are shown. Arrowheads: cells that did not proliferate during image acquisition.

(C) Live cell number at indicated time points after reseeding (mean ± SEM, $n = 2$ biological replicates). (D) Live cell number (left) and percentage of dead cells (right) 48 h after reseeding (mean ± SEM, $n = 2$ biological replicates). (E) Left: cells 48 h after reseeding were subjected to either cleaved caspase-3 staining (red). Blue: DNA. Arrowheads: cleaved caspase-3-positive cells. Right: cell number and percentage of cleaved caspase-3-positive cells per field (mean ± SEM, $n = 10$ fields from 2 independent experiments).

Scale bars, 100 μm. $^{**}p < 0.01$, $^{***}p < 0.001$, and $^{****}p < 0.0001$ (C: two-way ANOVA; D and E: one-way ANOVA).

See also Figure S2; Videos S1 and S2.

showed only minimal growth, while control and *PRL* single-KO cells exhibited steady increases in viable cell numbers (Figure 2C). We also performed *PRL* KO + KD with another siRNA targeting a different site of *PRL1* (*PRL1*-siRNA-2) and confirmed that it also effectively reduced PRL1 expression (Figure S2A) and suppressed the increase in viable cells (Figure S2B), as did *PRL1*-siRNA-1. Notably, the proportion of dead cells was drastically increased in *PRL* KO + KD cells (Figure 2D). Furthermore, immunofluorescence staining for cleaved caspase-3, a marker of apoptotic cells, showed a significant increase in *PRL* KO + KD cells (Figure 2E).

To evaluate the possibility that impaired proliferation may contribute to the reduced cell numbers in *PRL* KO + KD cells, we assessed DNA synthesis by 5-ethynyl-2′-deoxyuridine (EdU) incorporation assay. The fraction of S-phase cells was not significantly different between *PRL* KO + KD and control cells (Figure S2C). Time-lapse analysis of individual dividing cells revealed only a slight increase in cell cycle duration in *PRL* KO + KD cells (Figure S2D). Additionally, flow cytometry analysis showed a substantial accumulation of sub-G1 cells—indicative of cell death[42–44]—in PRL KO + KD cells (Figure S2E, 16%–23%). However, the distribution of G1, S, and G2/M phases among viable non-sub-G1 cells remained comparable across conditions, indicating that cell cycle progression was not markedly affected by *PRL* KO + KD. Collectively, these findings demonstrate that comprehensive suppression of PRL family proteins leads to massive cell death rather than impaired proliferation.

NF-κB activation downstream of intracellular Mg^{2+} decrease drives cell death

To investigate the mechanism underlying cell death induced by *PRL* KO + KD, we first assessed whether Mg^{2+} decrease is the actual trigger. Given that cellular Mg level was significantly reduced in *PRL* KO + KD cells, we supplemented culture media with excess Mg^{2+} (20 mM) and confirmed the significant increase in intracellular Mg levels (Figure 3A). The Mg^{2+} supplementation also significantly restored viable cell numbers and reduced the proportion of dead cells and cleaved caspase-3-positive cells

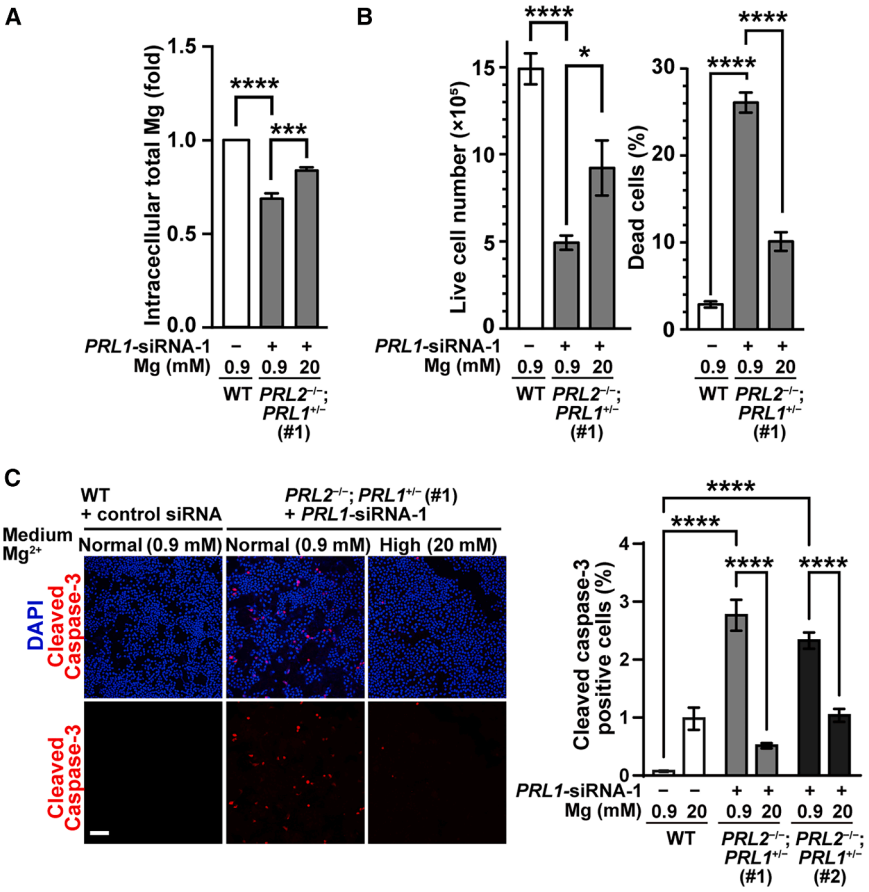

Figure 3. Mg^{2+} supplementation rescues cell death induced by PRL suppression

Indicated MDCK-derived cell lines were transfected twice with control siRNA ("−") or *PRL1*-siRNA-1 ("+") and cultured with normal culture medium containing 0.9 mM Mg^{2+} or medium supplemented with 20 mM Mg^{2+}. (A) Total intracellular Mg contents were quantified at 6 h after the second transfection with xylidyl blue (mean ± SEM, $n = 3$ biological replicates). (B) Live cell number (left) and percentage of dead cells (right) were counted 30 h after the second transfection (mean ± SEM, $n = 4–5$ biological replicates). (C) Cells were fixed 30 h after the second transfection and stained for cleaved caspase-3 (left, red). Blue: DNA. Right: percentage of cleaved caspase-3-positive cells per field (mean ± SEM, $n = 20$ fields from 2 independent experiments). Scale bars, 100 μm. $^{*}p < 0.05$, $^{***}p < 0.001$, and $^{****}p < 0.0001$ (one-way ANOVA).

under *PRL* KO + KD conditions (Figures 3B and 3C), confirming that intracellular Mg^{2+} decrease is a key driver of cell death in this condition.

We next performed transcriptomic analysis to profile the changes in global gene expression by *PRL* KO + KD (Figure 4A). A total of 295 genes were found to be upregulated >2-fold in *PRL* KO + KD cells (Figure 4B, left). Enrichment analysis identified related to NF-κB subunit RelA/p65[45] as the top candidate (Figure 4C). Indeed, 10 of the 16 genes upregulated >5-fold were known NF-κB targets, such as *CCL5* and *IL-6* (Figure 4B, right), suggesting robust activation of NF-κB signaling following PRL deletion and Mg^{2+} deprivation.

To validate NF-κB activation, we performed immunofluorescence staining of p65, a core subunit of the NF-κB complex, which translocates from cytosol to nucleus upon signal activation[45] (Figure S3A). While p65 was predominantly localized to the cytoplasm in control cells, *PRL* KO + KD induced a strong nuclear accumulation of p65 (arrowheads, Figure 5A), confirming NF-κB activation. Importantly, Mg^{2+} supplementation suppressed p65 translocation, indicating Mg^{2+} decrease as the upstream trigger of NF-κB activation.

To directly assess the role of NF-κB in cell death by *PRL* KO + KD, we next generated *p65*-KO cells derived from *PRL2*$^{-/-}$; *PRL1*$^{+/-}$ cells (referred to as *p65*$^{-/-}$; *PRL2*$^{-/-}$; *PRL1*$^{+/-}$, Figures 5B and 5C). *PRL1*-siRNA was then introduced into the two clones of *p65*$^{-/-}$; *PRL2*$^{-/-}$; *PRL1*$^{+/-}$ cells. In both clones, cell death was markedly suppressed, as shown by increased viable cell counts and decreased percentages of dead cells and cleaved caspase-3-positive cells (Figures 5D and 5E). Moreover, IMD-0354, a selective inhibitor of IKKβ, the kinase upstream of p65,[46] also effectively blocked p65 nuclear translocation and suppressed cell death and caspase-3 cleavage in *PRL* KO + KD cells (Figures S3C and S3D). Collectively, these findings demonstrate that intracellular Mg^{2+} decrease activates NF-κB signaling, which is both necessary to drive cell death following PRL deletion.

CNNM overexpression triggers NF-κB activation and cell death

In cellular Mg^{2+} handling, PRLs suppress CNNM-mediated Mg^{2+} efflux. Thus, we next interrogated whether Mg^{2+} decrease due to forced CNNM overexpression triggers NF-κB activation and subsequent cell death (Figure 6A). We focused on CNNM4, which has been reported to exhibit the strongest Mg^{2+} efflux activity among mammalian CNNM family members.[15] The overexpression of FLAG-tagged CNNM4 in WT MDCK cells caused a substantial increase in nuclear p65 localization and cleaved caspase-3-positive cells (Figures 6B and 6C). These effects were reversed by supplementing excess Mg^{2+} to the medium, indicating that intracellular Mg^{2+} decrease by CNNM4 overexpression also induced NF-κB activation and cell death.

To examine whether the Mg^{2+} decrease-dependent cell death is conserved across other cell types, we utilized HT-1080 human fibrosarcoma cells, which are commonly used in cell death studies.[47,48] We generated a cell clone stably expressing a doxycycline (DOX)-inducible CNNM4-FLAG expression (hereafter iCNNM4-FLAG cells, Figure 6D). Without DOX, the intracellular Mg level of iCNNM4-FLAG cells was

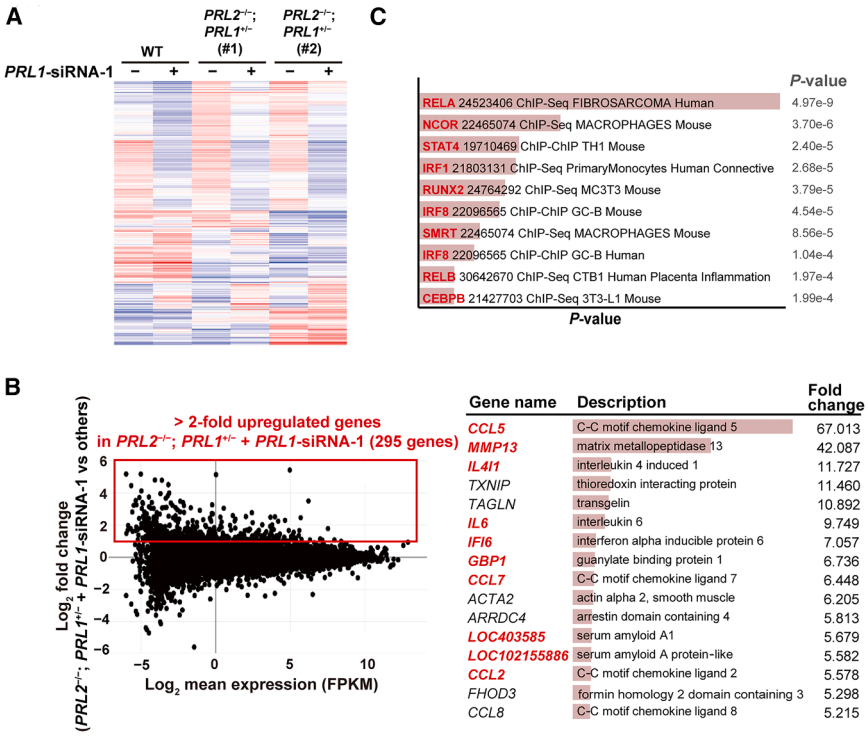

Figure 4. RNA-seq analysis of PRL-deprived cells reveals activation of the NF-κB pathway

RNAs were isolated from indicated MDCK-derived cell lines transfected twice with control siRNA ("−") or *PRL1*-siRNA-1 ("+") and subjected to RNA-seq analysis. (A) Heatmap showing up- (red) and downregulation (blue) of the top 1,000 most differentially expressed genes in the *PRL* KO + KD groups.

(B) Left: minus-average (MA) plot, representing the fold change in the $\log_2$ value between groups ("−," vertical) versus mean expression levels in $\log_2$ value ("average," horizontal) for each gene. Right, >5-fold upregulated genes with descriptions (middle) and fold change (right and bars). Red, genes reportedly upregulated by NF-κB activation.

(C) Top 10 transcription factors from enrichment analysis using the top 500 upregulated genes and the ChEA2022 database. Bars: significance level (−log10 of the *p* value).

comparable to that of WT cells. Upon CNNM induction by DOX treatment, intracellular total Mg levels dropped to approximately two-thirds of the baseline (Figure 6E). Doses of 0.1 μg/mL or higher induced near-complete cell death within 48 h (Figure 6F). The cell death was strongly suppressed by Mg^{2+} supplementation, mirroring the phenotype observed in *PRL* KO + KD MDCK cells (Figure 3). Consistently, DOX treatment led to the nuclear translocation of p65 in iCNNM4-FLAG cells (Figure 6G). The expression levels of IκBα, whose degradation is a marker of NF-κB activation,[45] decreased upon CNNM4 induction, though not as drastically as in response to TNF-α treatment (a canonical NF-κB activator) (Figure 6D). Collectively, these results indicate that the intracellular Mg^{2+} decrease induced by CNNM4 overexpression leads to NF-κB pathway activation and cell death.

Cellular Mg^{2+} decrease induces a non-canonical form of cell death

To further characterize the mode of cell death induced by cellular Mg^{2+} decrease, we tested the effects of pharmacological inhibitors targeting the major regulated cell death pathways: Z-VAD-FMK (apoptosis),[49] liproxstatin-1 (Lip-1, ferroptosis),[50] MCC950 or VX765 (pyroptosis),[51,52] and necrostatin-1 (Nec-1, necroptosis).[53] None of these compounds rescued cell viability in DOX-treated iCNNM4-FLAG cells (Figure 6F). *PRL* KO + KD cells and CNNM4-overexpressing cells exhibited cleaved caspase-3 positivity, which is considered a *bona fide* apoptosis marker (Figures 2E and 6C). Nonetheless, the emergence of lower levels of cleaved caspase-3 can be observed as a secondary event in other types of regulated cell death, such as ferroptosis and pyroptosis.[54–56] Cell death induced by Mg^{2+} decrease was not prevented even by the pan-caspase inhibitor Z-VAD-FMK, a broad-spectrum apoptosis inhibitor, suggesting that the conventional apoptotic pathway is unlikely to be involved.

Given prior links between NF-κB activation and pyroptosis,[57] we additionally examined gasdermin D (GSDMD) cleavage, a hallmark of pyroptotic execution.[58] As expected, GSDMD cleavage was detected in J774A.1 macrophages following pyroptosis induction by lipopolysaccharide and ATP stimulation (Figure S4A). In contrast, HT-1080 and MDCK cells showed only marginal GSDMD expression, and cleavage products were undetectable following CNNM4 overexpression or *PRL* KO + KD, respectively. Overall, these results suggest that a decrease in cellular Mg^{2+} triggers cell death distinct from conventional regulated cell death, such as apoptosis, ferroptosis, pyroptosis, and necroptosis. We also utilized RNA sequencing (RNA-seq) data (Figure 4) and analyzed genes with >2-fold downregulation by *PRL* KO + KD (239 genes). We compared them with the gene set "pro-survival," which contains inhibitory genes of the known regulated cell death but there was no significant overlap (Table S1). We also did not find significant overlap with genes known to be upregulated by the activation of prosurvival MAPK, Akt, and mTOR pathways but some components of these pathways were downregulated (Table S1).

We also tested the possible involvement of several known causes of cell death via NF-κB signal activation, such as excess/prolonged TNF-α exposure by the formation of a feed-forward autocrine loop[59] and oxidative/genotoxic stress[60] in Mg^{2+} decrease-dependent cell death. Supplementation of TNF-α-neutralizing antibody to the culture media failed to suppress cell death by CNNM4 induction (Figure S4B), excluding the possibility of cell death via excess/prolonged TNF-α exposure. As for the oxidative stress, we measured the intracellular

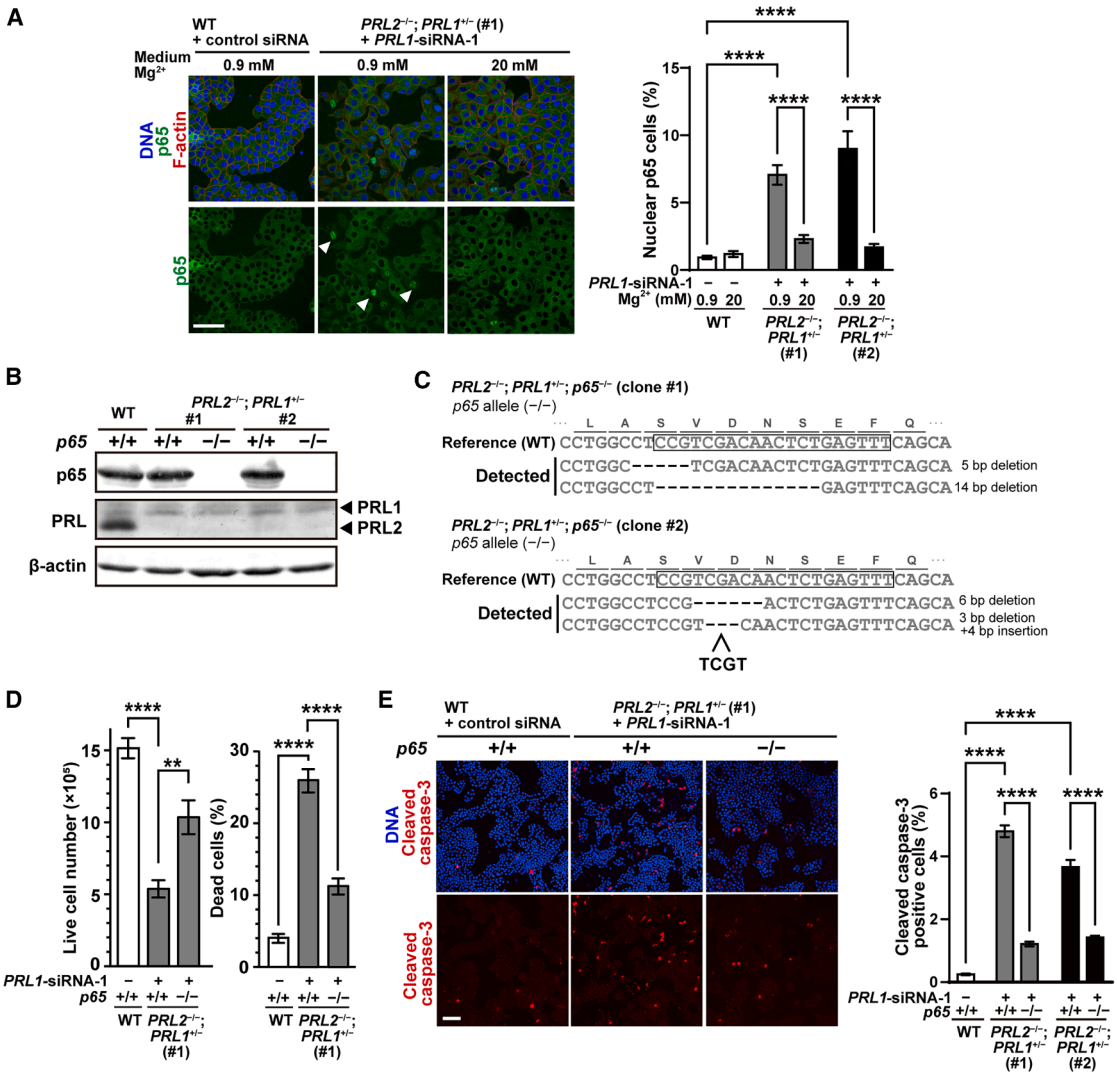

Figure 5. Targeted deletion of the p65 subunit of NF-κB rescues cell death

(A) Left, indicated MDCK-derived cells were transfected twice with control siRNA ("−") or *PRL1*-siRNA-1 ("+") and cultured with medium containing indicated Mg^{2+} concentrations. The cells were fixed 6 h after the second transfection and stained for p65 (left, green). Blue: DNA, red: F-actin. Scale bars, 50 μm. Nuclear p65 cells are marked with *arrowheads*. Right, percentage of nuclear p65 cells per field (mean ± SEM, n = 20 fields from 2 independent experiments).

(B) Lysates of indicated MDCK-derived cells were subjected to immunoblotting with the indicated antibodies.

(C) Genomic sequencing analysis of indicated MDCK-derived cell lines. Detected sequences are shown below the reference WT sequence. Boxed letters: sgRNA target sites. The amino acid sequence of WT p65 is also shown.

(D) Live cell number (left) and dead cell percentage (right) of the indicated MDCK-derived cells 30 h after the second transfection (mean ± SEM, n = 4–5 biological replicates).

(E) Left: indicated MDCK-derived cells were fixed 30 h after the second transfection and stained for cleaved caspase-3 (red). Blue: DNA. Right: percentage of cleaved caspase-3-positive cells per field (mean ± SEM, n = 19–20 fields from 2 independent experiments).

Scale bars, 50 μm (A) or 100 μm (E). $^{**}p < 0.01$ and $^{****}p < 0.0001$ (two-way ANOVA).

See also Figure S3.

levels of general reactive oxygen species (ROS) and H_2O_2 using fluorescent sensor molecules DCFH-DA and HyPer,[61] respectively, and found that neither increased in CNNM4-induced cells (Figures S4C and S4D). In contrast, immunofluorescence staining of γH2AX, a well-known marker of damaged DNA,[62] showed the emergence of γH2AX-positive foci in the nucleus of both CNNM4-induced cells and H_2O_2-treated cells (Figure S4E). Since ATM plays a crucial role in NF-κB signal activation upon DNA damage,[63,64] we treated cells with its inhibitor KU-55933. Cell death and p65 nuclear translocation by CNNM4-induction were not suppressed by KU-55933 treatment, suggesting that DNA damage is not related to the Mg^{2+} decrease-mediated activation of NF-κB signaling and subsequent induction of cell death (Figure S4F).

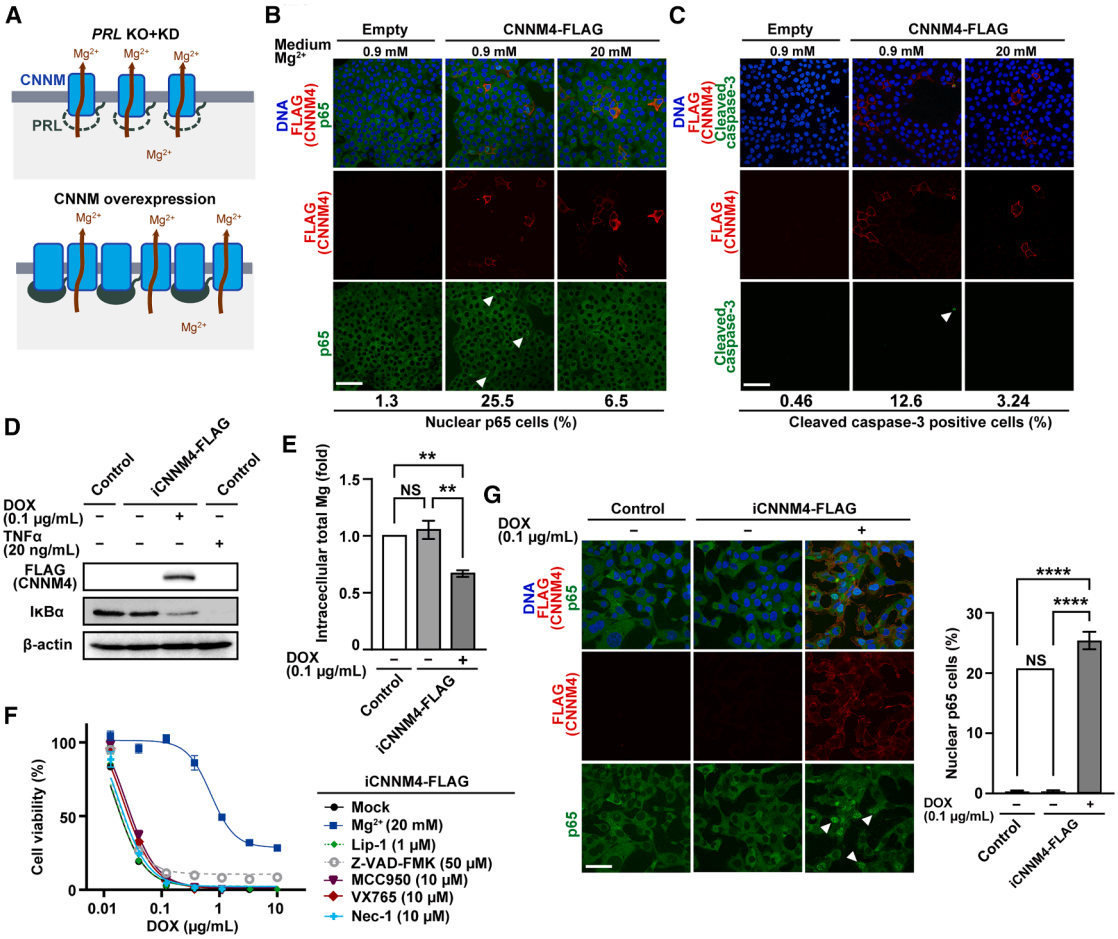

Figure 6. Overexpression of the Mg^{2+} exporter CNNM4 recapitulates features induced by near-complete suppression of RPL

(A) Schematic of intracellular Mg^{2+} decrease by *PRL* KO + KD and CNNM overexpression.

(B and C) WT MDCK cells were transfected with indicated expression constructs, fixed 30 h (B) or 36 h (C) after transfection, and stained for FLAG (red) and p65 (B, green) or cleaved caspase-3 (C, green). Blue: DNA. Cells with nuclear p65 localization (B) and positive for cleaved caspase-3 (C) are indicated with *arrowheads*, and their percentages relative to either total cells (for empty vector-transfected cells) or CNNM4-FLAG expressing cells are also indicated (n = [from left to right] 227, 216, 201, 217, 206, and 216).

(D–G) Indicated HT-1080-derived cell lines were cultured in the presence ("+") or absence ("−") of indicated DOX concentrations. (D) Lysates of cells 30 h after DOX treatment were subjected to immunoblotting with the indicated antibodies. Cells were treated with TNF-α for 30 min. (E) Total intracellular Mg contents at 30 h after DOX treatment were quantified using xylidyl blue (mean ± SEM, n = 3 biological replicates). (F) Cell viability after 48 h either with 20 mM Mg^{2+} supplementation or various compounds at indicated concentrations (mean ± SEM, n = 3 biological replicates). (G) Left: cells fixed 30 h after DOX treatment were stained for FLAG (red) and p65 (green). Blue: DNA. Cells with nuclear p65 localization were indicated with arrowheads. Right: percentage of nuclear p65 cells per field (mean ± SEM, n = 20 fields from 2 independent experiments).

Scale bars, 50 μm in (B and G) and 100 μm in (C). $^{**}p < 0.01$ and $^{****}p < 0.0001$; NS, not significant (E: one-way ANOVA and G: two-way ANOVA).

See also Figure S4 and Table S1.

Mg^{2+} decrease induces a morphologically distinct form of cell death characterized by actin-based elongated structures

Each form of regulated cell death exhibits distinct morphological changes.[65,66] To investigate the morphological features of Mg^{2+} decrease-induced cell death, we first analyzed iCNNM4-FLAG HT-1080 cells by phase-contrast microscopy (Figure 7A, Video S3). Upon CNNM4 induction by DOX, cells exhibited a characteristic morphological feature: following shrinkage and membrane blebbing, they formed numerous elongated, fiber-like structures (*arrowheads* in Figure 7A), which subsequently collapsed prior to cell rupture. To visualize these structures in greater detail, we employed holotomographic microscopy, which provides label-free imaging based on refractive index contrast.[67] During the cell death process, all observed cells (n = 20) formed elongated protrusions within 1 h of initial shrinkage and blebbing (Figure 7B, top; Video S4). Many protrusions extended beyond the original cell boundary (dotted lines in Figure 7B), indicating that these structures were not retraction fibers; the thin structure of membrane-substrate attachment remained after the retraction of cell boundaries.[68]

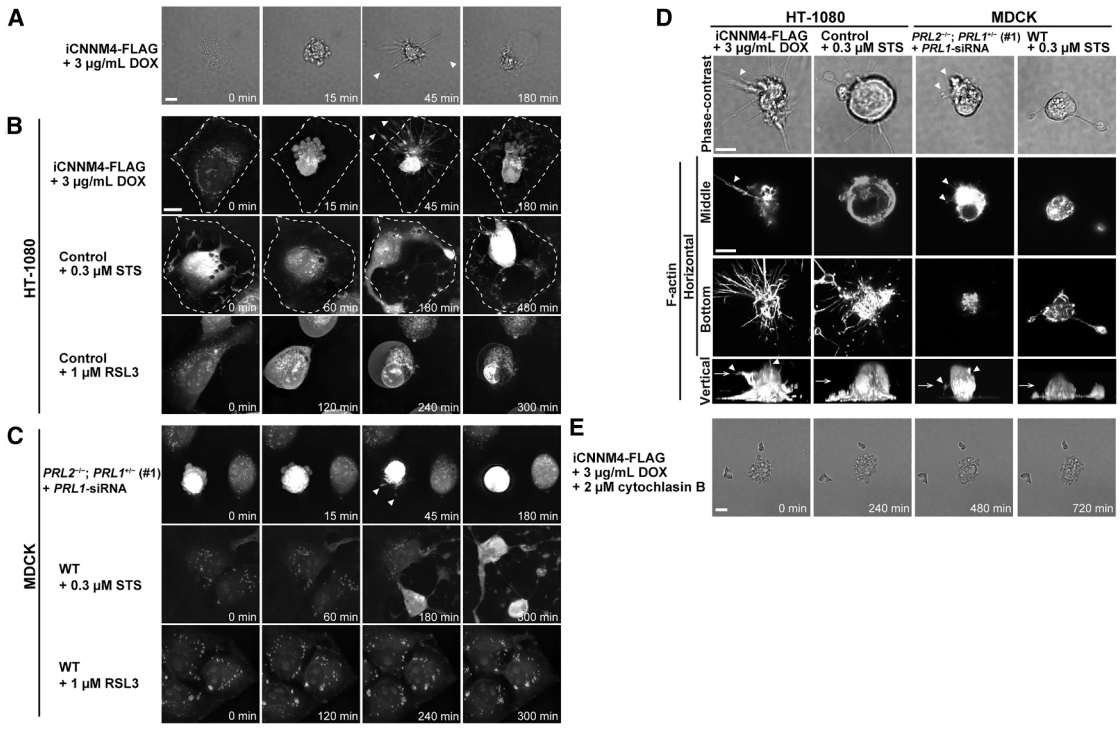

Figure 7. Mg^{2+} deprivation-induced cell death shows unique morphological features

(A) iCNNM4-FLAG cells (HT-1080 derived) were cultured in 3 μg/mL DOX for 24 h. Phase-contrast images were acquired every 1 min, and representative images at the indicated time points ("0 min" indicates the time point before cell shrinkage starts) are shown. Arrowheads: elongated structures.

(B–D) Indicated HT-1080-derived or MDCK-derived cell lines were either transfected twice with *PRL1*-siRNA-1 and reseeded ($PRL2^{-/-}$; $PRL1^{+/-}$ cells [#1]) or treated with indicated compounds (others). (B and C) Representative maximum intensity projection views of holotomographic images at the indicated timepoints. "0 min" indicates either the time point after the RSL3 treatment (WT MDCK cells + RSL3) or before the cell shrinkage starts (others). Arrowheads: elongated structures. *Dotted lines*: cell area at 0 min. (D) Cells were labeled for F-actin with siR-actin, and fluorescence images were acquired under a confocal scanning laser microscope. Corresponding phase-contrast images were acquired and shown with confocal fluorescence images of the bottom and middle horizontal sections. Side projection views from the 3D reconstituted images are also shown as vertical images. *Arrowheads*: elongated structures. *Arrows*: position of the middle horizontal section.

(E) iCNNM4-FLAG cells (HT-1080 derived) were cultured in 3 μg/mL DOX for 24 h. Blebbing cells were treated with cytochalasin B, and the phase-contrast images were acquired every 1 min. Representative images at the indicated time points are shown. 0 min is the time point after the cytochalasin B treatment.

Scale bars, 10 μm.

See also Figure S5; Table S2; and Videos S3, S4, S5, S6, S7, S8, S9, and S10.

To determine whether these features are specific to Mg^{2+} decrease-mediated death, we compared the morphology of cells treated with staurosporine (STS; apoptosis inducer) or RSL3 (ferroptosis inducer).[69,70] STS-treated cells also formed elongated structures, but these appeared during cell shrinkage and remained within the original cell area (Figure 7B, middle; Video S5). RSL3-treated cells exhibited balloon-like morphology without elongated projections (Figure 7B, bottom; Video S6). These results suggest that Mg^{2+} decrease-mediated cell death is morphologically distinct from both apoptosis and ferroptosis.

We then examined *PRL* KO + KD MDCK cells (Figure 7C, top; Video S7). Most of the cells (10 out of 14) developed similar elongated structures after blebbing. In contrast, STS-treated MDCK cells displayed typical apoptotic morphology: cell shrinkage and the resultant appearance of retraction fiber-like structures (Figure 7C, middle; Video S8). MDCK cells were resistant to RSL3 treatment and cell death was not observed (Figure 7C, bottom and Video S9).

To further characterize the nature of the elongated structures observed in Mg^{2+} decrease-mediated cell death, we performed live-cell confocal microscopy using SiR-actin, a fluorescent probe that detects the actin filament. Notably, in iCNNM4-FLAG HT-1080 cells, elongated structures were SiR-actin-positive and were present not only in the confocal plane at the bottom of the cells but also in the upper planes ("middle") (Figure 7D). Actin-positive protrusions above the basal plane were also observed in *PRL* KO + KD MDCK cells, but not in STS-treated cells. To exclude the possibility that the elongated structures were neutrophil extracellular traps (NETs),[71] we stained cells with a DNA labeling dye. However, no DNA signal was detected in the elongated structures (Figure S5), ruling out NETosis as their origin. Collectively, these results suggest that Mg^{2+} decrease-mediated cell death, triggered by either CNNM4 expression or *PRL* KO + KD, shows characteristic morphological features, including actin-driven, fiber-like protrusions.

Given the presence of actin filaments in the elongated structures, we tested the effect of cytochalasin B, an inhibitor of actin polymerization, on the formation of elongated structures and blebbing. Blebbing is generally driven by a cycle of transient detachment of the actin-cell membrane interaction and subsequent reconstruction of the actin filaments.[72] Notably, cytochalasin B treatment completely abolished the formation of elongated structures in all three time-lapse analyses (Figure 7E; Video S10). In addition, cytochalasin B treatment caused blebbing to persist throughout the 12-h imaging period, whereas in untreated cells, blebbing quickly resolved within 23.9 ± 1.2 min (n = 20; Figure 7A; Video S3). These results suggest the importance of actin polymerization not only for generating elongated structures but also for progression through the terminal phase of Mg^{2+} decrease-induced cell death process. Together, our findings reveal an actin-dependent cell death morphology distinct from known forms of regulated cell death.

DISCUSSION

In the present study, we investigated the physiological role of the PRL family in cellular Mg^{2+} homeostasis. By employing a combination of the KO and KD approaches targeting PRLs, we achieved near-complete suppression of PRL expression in MDCK cells. We revealed that intracellular Mg^{2+} decrease by PRL deletion or CNNM overexpression triggers an NF-κB-dependent cell death that exhibits characteristic morphological features, including actin-driven fiber-like protrusions.

Mechanistic analyses revealed that Mg^{2+} decrease-induced cell death, triggered either by *PRL* KO + KD or CNNM4 overexpression, involves activation of the NF-κB pathway. The impact of NF-κB activation on cell death is context-dependent. While it typically suppresses caspase-8- and caspase-3-mediated apoptosis or RIPK1-, RIPK3-, and MLKL-dependent necroptosis,[73,74] its aberrant activation can promote inflammasome and gasdermin D-mediated pyroptosis.[58] However, in our system, NF-κB acts as a pro-death mediator in the context of cellular Mg^{2+} deficiency, through a mechanism distinct from known cell death modalities including apoptosis, ferroptosis, pyroptosis, and necroptosis. The NF-κB pathway can be activated by diverse stimuli, including inflammatory cytokines, microbial products, and genotoxic stress,[75] all of which converge on the activation of the IKK complex, leading to IκBα degradation and p65 nuclear translocation. The suppression of *PRL* KO + KD-induced cell death by the IKKβ inhibitor IMD-0354 implicates IKK signaling as a downstream effector of Mg^{2+} decrease. Identifying Mg^{2+}-sensitive components upstream of IKK may provide insights into the signaling axis responsible for NF-κB-dependent cell death. Related to this point, we found the occurrence of genotoxic stress in CNNM4-induced cells but it is unlikely to be the cause of NF-κB activation and subsequent induction of cell death, since the cell death and p65 nuclear translocation were not suppressed by supplementing an inhibitor of ATM, the kinase crucial for NF-κB activation upon DNA damage. Further studies are therefore needed to clarify the cell death-promoting mechanism through NF-κB activation during Mg^{2+} decrease-mediated cell death.

Morphological analyses revealed that Mg^{2+} decrease-mediated cell death exhibited characteristic actin-based elongated protrusions that were distinct from those observed in other forms of regulated cell death. In addition, an actin polymerization inhibitor cytochalasin B abolished the formation of the elongated structures and delayed the resolution of blebbing. While actin dynamics are known to modulate multiple forms of cell death, our findings suggest that these actin-based protrusions may also play a functional role in signal amplification or cell disassembly in Mg^{2+} decrease-mediated cell death. Cytochalasin B treatment has been known to suppress the release of NET in NETosis.[76,77] Since the inhibition of actin polymerization suppressed not only the emergence of elongated structures but also the completion of Mg^{2+} decrease-mediated cell death in our study, the elongated structures might play analogous roles as NET, possibly in signal amplification or cell disassembly. Gene ontology (GO) analysis with RNA-seq data (Figure 4) showed that among genes upregulated or downregulated by *PRL* KO + KD (>2-fold), 4 of them are both related to the regulation of actin filament-based processes and listed as NF-κB target genes (Table S2). Notably, the upregulation of actin-bundling protein Fascin 1[78] and downregulation of actin-severing protein Scinderin[79] may account for the emergence of fiber-like protrusions upon intracellular Mg^{2+} decrease by bundling and stabilizing actin filaments, and further studies may clarify their contribution.

Cleaved caspase-3, a classical marker of apoptosis, was detected in cells undergoing Mg^{2+}-mediated death. However, caspase inhibition with Z-VAD-FMK failed to rescue cell viability. Moreover, classical apoptotic features such as nuclear fragmentation were absent, further suggesting that caspase activation is likely a secondary event following other types of cell death.[54–56]

In conclusion, our studies unveiled a distinct mode of cell death initiated by intracellular Mg^{2+} decrease, which is characterized by NF-κB activation and the formation of actin-dependent, fiber-like protrusions.

Limitations of the study

To decrease intracellular Mg^{2+} levels, we employed two strategies, *PRL* KO + KD and CNNM4 expression, both of which induce cell death characterized by NF-κB activation and cellular protrusions. However, the cell death rate by *PRL* KO + KD was markedly lower than that by CNNM4 expression, which achieved an almost 100% rate. Such a substantial difference is presumably due to the incomplete suppression of PRL expression by *PRL* KO + KD. Ideally, we should have generated *PRL2*/*PRL1* double-KO cells, instead of minimizing PRL expression by combined KO and KD approaches. To accomplish *PRL2*/*PRL1* double KO, more elaborate strategies may be required, such as the introduction of a Tet-off-type *PRL2*/*PRL1* rescue construct for cells to survive under the *PRL2*/*PRL1* double-KO background[80]; subsequent DOX addition halts PRL expression from the rescue construct and results in complete depletion of PRL expression.

As for the importance of NF-κB signaling in Mg^{2+} decrease-dependent cell death, we showed that both p65 nuclear translocation and cell death are triggered by *PRL* KO + KD or CNNM4 expression. We also demonstrated the requirement of p65 in cell death by generating and analyzing *p65*-KO cells. However, these data cannot distinguish the role of NF-κB signaling as a direct inducer of cell death or as a prerequisite, making cells prone to cell death. Live monitoring p65 localization over time

may solve these issues; if NF-κB signaling directly drives Mg^{2+} decrease-dependent cell death, the cell death should consistently follow p65 nuclear translocation within the same cell after a certain time interval. We have tried to generate cell lines stably expressing GFP-tagged p65 in the cytosol but failed to observe p65 nuclear translocation and cell death upon CNNM4 expression for unknown reasons. It has been pointed out that excess p65 expression disrupts the dynamics of p65[81] and, thus, analysis with more sophisticated methods, such as knockin of GFP to the endogenous p65 locus, would be required.

RESOURCE AVAILABILITY

Lead contact

Requests for further information and reagents may be directed to and will be fulfilled by the lead contact, Yosuke Funato (funato.yosuke.3i@kyoto-u.ac.jp).

Materials availability

All unique/stable reagents generated in this study are available from the lead contact upon request.

Data and code availability

- This paper does not report any original code.
- RNA-seq data have been deposited at the NCBI Gene Expression Omnibus (GEO) database as GEO: GSE309910 and are publicly available as of the date of publication.
- Any additional information required to reanalyze the data reported in this paper is available from the lead contact upon request.

ACKNOWLEDGMENTS

We thank Dr. Yasuyuki Fujita (Kyoto University) for sharing MDCK cells. We also appreciate the NGS core facility of the Genome Information Research Center at the Research Institute for Microbial Diseases (Osaka University) for support in RNA sequencing and data analysis and Dr. Sweksha Lohani (RIKEN), Ms. Yayoi Tsumori (Kyoto University), and Ms. Yoshie Koyama (Kyoto University) for technical support. This work was supported by JSPS KAKENHI grant nos. JP21H05272, JP23H00409, and JP23K20040 to H.M. and JP24K02225 and JP25H01335 to Y.F.; JST SPRING program, grant no. JPMJSP2110 to K.K.; and JST FOREST program, grant no. JPMJFR216A to Y.F. M.C. received funding from the European Research Council (ERC) under the European Union's Horizon 2020 research and innovation program (grant agreement no. GA 884754).

AUTHOR CONTRIBUTIONS

K.K., H.M., and Y.F. conceived the study design. K.K. performed the experiments and analyzed the data, with contributions from K.O., E.M., O.H., M.C., and Y.F. K.K., E.M., M.C., H.M., and Y.F. wrote the manuscript. All the authors have read and confirmed the final version of the manuscript.

DECLARATION OF INTERESTS

M.C. is a co-founder and shareholder of ROSCUE Therapeutics GmbH.

STAR★METHODS

Detailed methods are provided in the online version of this paper and include the following:

- KEY RESOURCES TABLE
- EXPERIMENTAL MODEL AND STUDY PARTICIPANT DETAILS
- METHOD DETAILS
  - Cell culture and transient transfection
  - Generation of expression constructs
  - Generation of KO cell lines
  - Transient KD experiments
  - Generation of inducible C-terminal FLAG tagged CNNM4 (CNNM4-FLAG)-expressing cell lines
  - Cell counting
  - Quantification of intracellular Mg
  - Labeling of S-phase cells
  - Cell cycle analysis
  - Immunofluorescence microscopy
  - Live cell imaging
  - RNA-seq analysis
  - Quantification of intracellular H_2O_2 level using HyPer
  - Measurement of general ROS level using DCFH-DA
- QUANTIFICATION AND STATISTICAL ANALYSIS

SUPPLEMENTAL INFORMATION

Supplemental information can be found online at https://doi.org/10.1016/j.celrep.2026.116964.

Received: September 2, 2025
Revised: December 10, 2025
Accepted: January 13, 2026
Published: February 10, 2026

REFERENCES

1. de Baaij, J.H.F., Hoenderop, J.G.J., and Bindels, R.J.M. (2015). Magnesium in man: implications for health and disease. Physiol. Rev. *95*, 1–46. https://doi.org/10.1152/physrev.00012.2014.
2. Kolisek, M., Nestler, A., Vormann, J., and Schweigel-Röntgen, M. (2012). Human gene *SLC41A1* encodes for the Na^+/Mg^{2+} exchanger. Am. J. Physiol. Cell Physiol. *302*, C318–C326. https://doi.org/10.1152/ajpcell.00289.2011.
3. Smith, R.L., Thompson, L.J., and Maguire, M.E. (1995). Cloning and characterization of MgtE, a putative new class of Mg^{2+} transporter from *Bacillus firmus* OF4. J. Bacteriol. *177*, 1233–1238. https://doi.org/10.1128/jb.177.5.1233-1238.1995.
4. Yamazaki, D., Funato, Y., Miura, J., Sato, S., Toyosawa, S., Furutani, K., Kurachi, Y., Omori, Y., Furukawa, T., Tsuda, T., et al. (2013). Basolateral Mg^{2+} Extrusion via CNNM4 Mediates Transcellular Mg^{2+} Transport across Epithelia: A Mouse Model. PLoS Genet. *9*, e1003983. https://doi.org/10.1371/journal.pgen.1003983.
5. Gibson, M.M., Bagga, D.A., Miller, C.G., and Maguire, M.E. (1991). Magnesium transport in *Salmonella typhimurium*: the influence of new mutations conferring Co^{2+} resistance on the CorA Mg^{2+} transport system. Mol. Microbiol. *5*, 2753–2762. https://doi.org/10.1111/j.1365-2958.1991.tb01984.x.
6. Romani, A.M.P. (2011). Cellular magnesium homeostasis. Arch. Biochem. Biophys. *512*, 1–23. https://doi.org/10.1016/j.abb.2011.05.010.
7. Schlingmann, K.P., Weber, S., Peters, M., Niemann Nejsum, L., Vitzthum, H., Klingel, K., Kratz, M., Haddad, E., Ristoff, E., Dinour, D., et al. (2002). Hypomagnesemia with secondary hypocalcemia is caused by mutations in TRPM6, a new member of the TRPM gene family. Nat. Genet. *31*, 166–170. https://doi.org/10.1038/ng889.
8. Walder, R.Y., Landau, D., Meyer, P., Shalev, H., Tsolia, M., Borochowitz, Z., Boettger, M.B., Beck, G.E., Englehardt, R.K., Carmi, R., and Sheffield, V.C. (2002). Mutation of *TRPM6* causes familial hypomagnesemia with secondary hypocalcemia. Nat. Genet. *31*, 171–174. https://doi.org/10.1038/ng901.
9. Voets, T., Nilius, B., Hoefs, S., van der Kemp, A.W.C.M., Droogmans, G., Bindels, R.J.M., and Hoenderop, J.G.J. (2004). TRPM6 forms the Mg^{2+} influx channel involved in intestinal and renal Mg^{2+} absorption. J. Biol. Chem. *279*, 19–25. https://doi.org/10.1074/jbc.m311201200.
10. Runnels, L.W., Yue, L., and Clapham, D.E. (2001). TRP-PLIK, a bifunctional protein with kinase and ion channel activities. Science *291*, 1043–1047. https://doi.org/10.1126/science.1058519.

11. Zhou, H., and Clapham, D.E. (2009). Mammalian MagT1 and TUSC3 are required for cellular magnesium uptake and vertebrate embryonic development. Proc. Natl. Acad. Sci. USA *106*, 15750–15755. https://doi.org/10.1073/pnas.0908332106.

12. Kolisek, M., Zsurka, G., Samaj, J., Weghuber, J., Schweyen, R.J., and Schweigel, M. (2003). Mrs2p is an essential component of the major electrophoretic Mg^{2+} influx system in mitochondria. EMBO J. *22*, 1235–1244. https://doi.org/10.1093/emboj/cdg122.

13. Hmiel, S.P., Snavely, M.D., Miller, C.G., and Maguire, M.E. (1986). Magnesium transport in *Salmonella typhimurium*: characterization of magnesium influx and cloning of a transport gene. J. Bacteriol. *168*, 1444–1450. https://doi.org/10.1128/jb.168.3.1444-1450.1986.

14. Funato, Y., Yamazaki, D., Mizukami, S., Du, L., Kikuchi, K., and Miki, H. (2014). Membrane protein CNNM4-dependent Mg^{2+} efflux suppresses tumor progression. J. Clin. Investig. *124*, 5398–5410. https://doi.org/10.1172/jci76614.

15. Hirata, Y., Funato, Y., Takano, Y., and Miki, H. (2014). Mg^{2+}-dependent interactions of ATP with the cystathionine-β-synthase (CBS) domains of a magnesium transporter. J. Biol. Chem. *289*, 14731–14739. https://doi.org/10.1074/jbc.m114.551176.

16. Gulerez, I., Funato, Y., Wu, H., Yang, M., Kozlov, G., Miki, H., and Gehring, K. (2016). Phosphocysteine in the PRL-CNNM pathway mediates magnesium homeostasis. EMBO Rep. *17*, 1890–1900. https://doi.org/10.15252/embr.201643393.

17. Funato, Y., Yamazaki, D., and Miki, H. (2017). Renal function of cyclin M2 Mg^{2+} transporter maintains blood pressure. J. Hypertens. *35*, 585–592. https://doi.org/10.1097/hjh.0000000000001211.

18. Trachsel, E., Redder, P., Linder, P., and Armitano, J. (2019). Genetic screens reveal novel major and minor players in magnesium homeostasis of *Staphylococcus aureus*. PLoS Genet. *15*, e1008336. https://doi.org/10.1371/journal.pgen.1008336.

19. Huang, Y., Jin, F., Funato, Y., Xu, Z., Zhu, W., Wang, J., Sun, M., Zhao, Y., Yu, Y., Miki, H., and Hattori, M. (2021). Structural basis for the Mg^{2+} recognition and regulation of the CorC Mg^{2+} transporter. Sci. Adv. *7*, eabe6140. https://doi.org/10.1126/sciadv.abe6140.

20. Chen, Y.S., Kozlov, G., Moeller, B.E., Rohaim, A., Fakih, R., Roux, B., Burke, J.E., and Gehring, K. (2021). Crystal structure of an archaeal CorB magnesium transporter. Nat. Commun. *12*, 4028. https://doi.org/10.1038/s41467-021-24282-7.

21. Bai, Z., Feng, J., Franken, G.A.C., Al'Saadi, N., Cai, N., Yu, A.S., Lou, L., Komiya, Y., Hoenderop, J.G.J., de Baaij, J.H.F., et al. (2021). CNNM proteins selectively bind to the TRPM7 channel to stimulate divalent cation entry into cells. PLoS Biol. *19*, e3001496. https://doi.org/10.1371/journal.pbio.3001496.

22. Gil, S., Feord, H.K., and van Ooijen, G. (2023). Homologs of Ancestral CNNM Proteins Affect Magnesium Homeostasis and Circadian Rhythmicity in a Model Eukaryotic Cell. Int. J. Mol. Sci. *24*, 2273. https://doi.org/10.3390/ijms24032273.

23. Hardy, S., Uetani, N., Wong, N., Kostantin, E., Labbé, D.P., Bégin, L.R., Mes-Masson, A., Miranda-Saavedra, D., and Tremblay, M.L. (2015). The protein tyrosine phosphatase PRL-2 interacts with the magnesium transporter CNNM3 to promote oncogenesis. Oncogene *34*, 986–995. https://doi.org/10.1038/onc.2014.33.

24. Funato, Y., Hashizume, O., and Miki, H. (2023). Phosphatase-independent role of phosphatase of regenerating liver in cancer progression. Cancer Sci. *114*, 25–33. https://doi.org/10.1111/cas.15625.

25. Diamond, R.H., Cressman, D.E., Laz, T.M., Abrams, C.S., and Taub, R. (1994). PRL-1, a unique nuclear protein tyrosine phosphatase, affects cell growth. Mol. Cell Biol. *14*, 3752–3762. https://doi.org/10.1128/mcb.14.6.3752-3762.1994.

26. Saha, S., Bardelli, A., Buckhaults, P., Velculescu, V.E., Rago, C., St Croix, B., Romans, K.E., Choti, M.A., Lengauer, C., Kinzler, K.W., and Vogelstein, B. (2001). A phosphatase associated with metastasis of colorectal cancer. Science *294*, 1343–1346. https://doi.org/10.1126/science.1065817.

27. Bessette, D.C., Qiu, D., and Pallen, C.J. (2008). PRL PTPs: mediators and markers of cancer progression. Cancer Metastasis Rev. *27*, 231–252. https://doi.org/10.1007/s10555-008-9121-3.

28. Kozlov, G., Funato, Y., Chen, Y.S., Zhang, Z., Illes, K., Miki, H., and Gehring, K. (2020). PRL3 pseudophosphatase activity is necessary and sufficient to promote metastatic growth. J. Biol. Chem. *295*, 11682–11692. https://doi.org/10.1074/jbc.ra120.014464.

29. Ishii, T., Funato, Y., Hashizume, O., Yamazaki, D., Hirata, Y., Nishiwaki, K., Kono, N., Arai, H., and Miki, H. (2016). Mg^{2+} extrusion from intestinal epithelia by CNNM proteins is essential for gonadogenesis via AMPK-TORC1 signaling in *Caenorhabditis elegans*. PLoS Genet. *12*, e1006276. https://doi.org/10.1371/journal.pgen.1006276.

30. Yamazaki, D., Hasegawa, A., Funato, Y., Tran, H.N., Mori, M.X., Mori, Y., Sato, T., and Miki, H. (2019). *Cnnm4* deficiency suppresses Ca^{2+} signaling and promotes cell proliferation in the colon epithelia. Oncogene *38*, 3962–3969. https://doi.org/10.1038/s41388-019-0682-0.

31. Hashizume, O., Funato, Y., Yamazaki, D., and Miki, H. (2020). Excessive Mg^{2+} Impairs Intestinal Homeostasis by Enhanced Production of ATP and Reactive Oxygen Species. Antioxid. Redox Signal. *33*, 20–34. https://doi.org/10.1089/ars.2019.7951.

32. Funato, Y., Yoshida, A., Hirata, Y., Hashizume, O., Yamazaki, D., and Miki, H. (2020). The Oncogenic PRL Protein Causes Acid Addiction of Cells by Stimulating Lysosomal Exocytosis. Dev. Cell *55*, 387–397.e8. https://doi.org/10.1016/j.devcel.2020.08.009.

33. Hashizume, O., Kawabe, T., Funato, Y., and Miki, H. (2024). Intestinal Mg^{2+} accumulation induced by *cnnm* mutations decreases the body size by suppressing TORC2 signaling in *Caenorhabditis elegans*. Dev. Biol. *509*, 59–69. https://doi.org/10.1016/j.ydbio.2024.02.007.

34. Bai, Y., Zhou, H.M., Zhang, L., Dong, Y., Zeng, Q., Shou, W., and Zhang, Z.Y. (2016). Role of phosphatase of regenerating liver 1 (PRL1) in spermatogenesis. Sci. Rep. *6*, 34211. https://doi.org/10.1038/srep34211.

35. Zimmerman, M.W., Homanics, G.E., and Lazo, J.S. (2013). Targeted deletion of the metastasis-associated phosphatase *Ptp4a3* (PRL-3) suppresses murine colon cancer. PLoS One *8*, e58300. https://doi.org/10.1371/journal.pone.0058300.

36. Dong, Y., Zhang, L., Zhang, S., Bai, Y., Chen, H., Sun, X., Yong, W., Li, W., Colvin, S.C., Rhodes, S.J., et al. (2012). Phosphatase of regenerating liver 2 (PRL2) is essential for placental development by down-regulating PTEN (Phosphatase and Tensin Homologue Deleted on Chromosome 10) and activating Akt protein. J. Biol. Chem. *287*, 32172–32179. https://doi.org/10.1074/jbc.m112.393462.

37. Uetani, N., Hardy, S., Gravel, S.P., Kiessling, S., Pietrobon, A., Wong, N.N., Chénard, V., Cermakian, N., St-Pierre, J., and Tremblay, M.L. (2017). PRL2 links magnesium flux and sex-dependent circadian metabolic rhythms. JCI Insight *2*, e91722. https://doi.org/10.1172/jci.insight.91722.

38. Urwyler, O., Izadifar, A., Vandenbogaerde, S., Sachse, S., Misbaer, A., and Schmucker, D. (2019). Branch-restricted localization of phosphatase Prl-1 specifies axonal synaptogenesis domains. Science *364*, eaau9952. https://doi.org/10.1126/science.aau9952.

39. Yoshida, A., Funato, Y., and Miki, H. (2018). Phosphatase of regenerating liver maintains cellular magnesium homeostasis. Biochem. J. *475*, 1129–1139. https://doi.org/10.1042/bcj20170756.

40. Stephens, B., Han, H., Hostetter, G., Demeure, M.J., and Von Hoff, D.D. (2008). Small interfering RNA-mediated knockdown of PRL phosphatases results in altered Akt phosphorylation and reduced clonogenicity of pancreatic cancer cells. Mol. Cancer Ther. *7*, 202–210. https://doi.org/10.1158/1535-7163.mct-07-0542.

41. Hardy, S., Kostantin, E., Wang, S.J., Hristova, T., Galicia-Vázquez, G., Baranov, P.V., Pelletier, J., and Tremblay, M.L. (2019). Magnesium-sensitive upstream ORF controls PRL phosphatase expression to mediate

energy metabolism. Proc. Natl. Acad. Sci. USA *116*, 2925–2934. https://doi.org/10.1073/pnas.1815361116.

42. Darzynkiewicz, Z., Bruno, S., Del Bino, G., Gorczyca, W., Hotz, M.A., Lassota, P., and Traganos, F. (1992). Features of apoptotic cells measured by flow cytometry. Cytometry *13*, 795–808. https://doi.org/10.1002/cyto.990130802.
43. Tischner, D., Manzl, C., Soratroi, C., Villunger, A., and Krumschnabel, G. (2012). Necrosis-like death can engage multiple pro-apoptotic Bcl-2 protein family members. Apoptosis *17*, 1197–1209. https://doi.org/10.1007/s10495-012-0756-8.
44. Yang, Y., Liu, T., Hu, C., Xia, H., Liu, W., Chen, J., Wu, S., Jiang, Y., Xu, Y., Liu, W., and Zhao, L. (2021). Ferroptosis inducer erastin downregulates androgen receptor and its splice variants in castration-resistant prostate cancer. Oncol. Rep. *45*, 25. https://doi.org/10.3892/or.2021.7976.
45. Taniguchi, K., and Karin, M. (2018). NF-κB, inflammation, immunity and cancer: coming of age. Nat. Rev. Immunol. *18*, 309–324. https://doi.org/10.1038/nri.2017.142.
46. Tanaka, A., Konno, M., Muto, S., Kambe, N., Morii, E., Nakahata, T., Itai, A., and Matsuda, H. (2005). A novel NF-kappaB inhibitor, IMD-0354, suppresses neoplastic proliferation of human mast cells with constitutively activated c-kit receptors. Blood *105*, 2324–2331. https://doi.org/10.1182/blood-2004-08-3247.
47. Haga, N., Fujita, N., and Tsuruo, T. (2003). Mitochondrial aggregation precedes cytochrome c release from mitochondria during apoptosis. Oncogene *22*, 5579–5585. https://doi.org/10.1038/sj.onc.1206576.
48. Dixon, S.J., Lemberg, K.M., Lamprecht, M.R., Skouta, R., Zaitsev, E.M., Gleason, C.E., Patel, D.N., Bauer, A.J., Cantley, A.M., Yang, W.S., et al. (2012). Ferroptosis: an iron-dependent form of nonapoptotic cell death. Cell *149*, 1060–1072. https://doi.org/10.1016/j.cell.2012.03.042.
49. Slee, E.A., Zhu, H., Chow, S.C., MacFarlane, M., Nicholson, D.W., and Cohen, G.M. (1996). Benzyloxycarbonyl-Val-Ala-Asp (OMe) fluoromethylketone (Z-VAD.FMK) inhibits apoptosis by blocking the processing of CPP32. Biochem. J. *315*, 21–24. https://doi.org/10.1042/bj3150021.
50. Friedmann Angeli, J.P., Schneider, M., Proneth, B., Tyurina, Y.Y., Tyurin, V.A., Hammond, V.J., Herbach, N., Aichler, M., Walch, A., Eggenhofer, E., et al. (2014). Inactivation of the ferroptosis regulator Gpx4 triggers acute renal failure in mice. Nat. Cell Biol. *16*, 1180–1191. https://doi.org/10.1038/ncb3064.
51. Coll, R.C., Robertson, A.A.B., Chae, J.J., Higgins, S.C., Muñoz-Planillo, R., Inserra, M.C., Vetter, I., Dungan, L.S., Monks, B.G., Stutz, A., et al. (2015). A small-molecule inhibitor of the NLRP3 inflammasome for the treatment of inflammatory diseases. Nat. Med. *21*, 248–255. https://doi.org/10.1038/nm.3806.
52. Wannamaker, W., Davies, R., Namchuk, M., Pollard, J., Ford, P., Ku, G., Decker, C., Charifson, P., Weber, P., Germann, U.A., et al. (2007). (S)-1-((S)-2-{[1-(4-amino-3-chloro-phenyl)-methanoyl]-amino}-3,3-dimethyl-butanoyl)-pyrrolidine-2-carboxylic acid ((2R,3S)-2-ethoxy-5-oxo-tetrahydro-furan-3-yl)-amide (VX-765), an orally available selective interleukin (IL)-converting enzyme/caspase-1 inhibitor, exhibits potent anti-inflammatory activities by inhibiting the release of IL-1beta and IL-18. J. Pharmacol. Exp. Ther. *321*, 509–516. https://doi.org/10.1124/jpet.106.111344.
53. Degterev, A., Huang, Z., Boyce, M., Li, Y., Jagtap, P., Mizushima, N., Cuny, G.D., Mitchison, T.J., Moskowitz, M.A., and Yuan, J. (2005). Chemical inhibitor of nonapoptotic cell death with therapeutic potential for ischemic brain injury. Nat. Chem. Biol. *1*, 112–119. https://doi.org/10.1038/nchembio711.
54. Yu, Y., Xie, Y., Cao, L., Yang, L., Yang, M., Lotze, M.T., Zeh, H.J., Kang, R., and Tang, D. (2015). The ferroptosis inducer erastin enhances sensitivity of acute myeloid leukemia cells to chemotherapeutic agents. Mol. Cell. Oncol. *2*, e1054549. https://doi.org/10.1080/23723556.2015.1054549.
55. Campos, J., Gleitze, S., Hidalgo, C., and Núñez, M.T. (2024). IP3R-Mediated Calcium Release Promotes Ferroptotic Death in SH-SY5Y Neuroblastoma Cells. Antioxidants *13*, 196. https://doi.org/10.3390/antiox13020196.
56. Zeng, C.Y., Li, C.G., Shu, J.X., Xu, L.H., Ouyang, D.Y., Mai, F.Y., Zeng, Q.Z., Zhang, C.C., Li, R.M., and He, X.H. (2019). ATP induces caspase-3/gasdermin E-mediated pyroptosis in NLRP3 pathway-blocked murine macrophages. Apoptosis *24*, 703–717. https://doi.org/10.1007/s10495-019-01551-x.
57. Yang, L., Zhang, Y., Chai, Z., Zhou, Y., Li, Z., and Wei, Y. (2025). Regulation of pyroptosis by NF-κB signaling. Front. Cell Death *3*, 1503799. https://doi.org/10.3389/fceld.2024.1503799.
58. Shi, J., Zhao, Y., Wang, K., Shi, X., Wang, Y., Huang, H., Zhuang, Y., Cai, T., Wang, F., and Shao, F. (2015). Cleavage of GSDMD by inflammatory caspases determines pyroptotic cell death. Nature *526*, 660–665. https://doi.org/10.1038/nature15514.
59. Brenner, D., Blaser, H., and Mak, T.W. (2015). Regulation of tumour necrosis factor signalling: live or let die. Nat. Rev. Immunol. *15*, 362–374. https://doi.org/10.1038/nri3834.
60. Radhakrishnan, S.K., and Kamalakaran, S. (2006). Pro-apoptotic role of NF-kappaB: implications for cancer therapy. Biochim. Biophys. Acta *1766*, 53–62. https://doi.org/10.1016/j.bbcan.2006.02.001.
61. Oparka, M., Walczak, J., Malinska, D., van Oppen, L.M.P.E., Szczepanowska, J., Koopman, W.J.H., and Wieckowski, M.R. (2016). Quantifying ROS levels using CM-H2DCFDA and HyPer. Methods *109*, 3–11. https://doi.org/10.1016/j.ymeth.2016.06.008.
62. Rogakou, E.P., Boon, C., Redon, C., and Bonner, W.M. (1999). Megabase chromatin domains involved in DNA double-strand breaks *in vivo*. J. Cell Biol. *146*, 905–916. https://doi.org/10.1083/jcb.146.5.905.
63. Lee, S.J., Dimtchev, A., Lavin, M.F., Dritschilo, A., and Jung, M. (1998). A novel ionizing radiation-induced signaling pathway that activates the transcription factor NF-kappaB. Oncogene *17*, 1821–1826. https://doi.org/10.1038/sj.onc.1202088.
64. Wu, Z.H., and Miyamoto, S. (2008). Induction of a pro-apoptotic ATM-NF-kappaB pathway and its repression by ATR in response to replication stress. EMBO J. *27*, 1963–1973. https://doi.org/10.1038/emboj.2008.127.
65. Green, D.R. (2019). The Coming Decade of Cell Death Research: Five Riddles. Cell *177*, 1094–1107. https://doi.org/10.1016/j.cell.2019.04.024.
66. Mishima, E., Nakamura, T., Doll, S., Proneth, B., Fedorova, M., Pratt, D.A., Friedmann Angeli, J.P., Dixon, S.J., Wahida, A., and Conrad, M. (2025). Recommendations for robust and reproducible research on ferroptosis. Nat. Rev. Mol. Cell Biol. *26*, 615–630. https://doi.org/10.1038/s41580-025-00843-2.
67. Kim, D., Lee, S., Lee, M., Oh, J., Yang, S.A., and Park, Y. (2021). Holotomography: Refractive Index as an Intrinsic Imaging Contrast for 3-D Label-Free Live Cell Imaging. Adv. Exp. Med. Biol. *1310*, 211–238. https://doi.org/10.1007/978-981-33-6064-8_10.
68. Mitchison, T.J. (1992). Actin based motility on retraction fibers in mitotic PtK2 cells. Cell Motil Cytoskeleton *22*, 135–151. https://doi.org/10.1002/cm.970220207.
69. Bertrand, R., Solary, E., O'Connor, P., Kohn, K.W., and Pommier, Y. (1994). Induction of a common pathway of apoptosis by staurosporine. Exp. Cell Res. *211*, 314–321. https://doi.org/10.1006/excr.1994.1093.
70. Yang, W.S., SriRamaratnam, R., Welsch, M.E., Shimada, K., Skouta, R., Viswanathan, V.S., Cheah, J.H., Clemons, P.A., Shamji, A.F., Clish, C.B., et al. (2014). Regulation of ferroptotic cancer cell death by GPX4. Cell *156*, 317–331. https://doi.org/10.1016/j.cell.2013.12.010.
71. Vorobjeva, N.V., and Chernyak, B.V. (2020). NETosis: Molecular Mechanisms, Role in Physiology and Pathology. Biochemistry. *85*, 1178–1190. https://doi.org/10.1134/s0006297920100065.
72. Charras, G.T. (2008). A short history of blebbing. J. Microsc. *231*, 466–478. https://doi.org/10.1111/j.1365-2818.2008.02059.x.
73. Luo, J.L., Kamata, H., and Karin, M. (2005). IKK/NF-kappaB signaling: balancing life and death–a new approach to cancer therapy. J. Clin. Investig. *115*, 2625–2632. https://doi.org/10.1172/jci26322.

74. Ting, A.T., and Bertrand, M.J.M. (2016). More to Life than NF-κB in TNFR1 Signaling. Trends Immunol. *37*, 535–545. https://doi.org/10.1016/j.it.2016.06.002.

75. Guo, Q., Jin, Y., Chen, X., Ye, X., Shen, X., Lin, M., Zeng, C., Zhou, T., and Zhang, J. (2024). NF-κB in biology and targeted therapy: new insights and translational implications. Signal Transduct. Target. Ther. *9*, 53. https://doi.org/10.1038/s41392-024-01757-9.

76. Neeli, I., Dwivedi, N., Khan, S., and Radic, M. (2009). Regulation of extracellular chromatin release from neutrophils. J. Innate Immun. *1*, 194–201. https://doi.org/10.1159/000206974.

77. Neubert, E., Meyer, D., Rocca, F., Günay, G., Kwaczala-Tessmann, A., Grandke, J., Senger-Sander, S., Geisler, C., Egner, A., Schön, M.P., et al. (2018). Chromatin swelling drives neutrophil extracellular trap release. Nat. Commun. *9*, 3767. https://doi.org/10.1038/s41467-018-06263-5.

78. Bryan, J., and Kane, R.E. (1978). Separation and interaction of the major components of sea urchin actin gel. J. Mol. Biol. *125*, 207–224. https://doi.org/10.1016/0022-2836(78)90345-5.

79. Rodriguez Del Castillo, A., Lemaire, S., Tchakarov, L., Jeyapragasan, M., Doucet, J.P., Vitale, M.L., and Trifaró, J.M. (1990). Chromaffin cell scinderin, a novel calcium-dependent actin filament-severing protein. EMBO J. *9*, 43–52. https://doi.org/10.1002/j.1460-2075.1990.tb08078.x.

80. Wang, B., Wang, Z., Wang, D., Zhang, B., Ong, S.G., Li, M., Yu, W., and Wang, Y. (2019). krCRISPR: an easy and efficient strategy for generating conditional knockout of essential genes in cells. J. Biol. Eng. *13*, 35. https://doi.org/10.1186/s13036-019-0150-y.

81. Kizilirmak, C., Bianchi, M.E., and Zambrano, S. (2022). Insights on the NF-κB System Using Live Cell Imaging: Recent Developments and Future Perspectives. Front. Immunol. *13*, 886127. https://doi.org/10.3389/fimmu.2022.886127.

82. Mishima, E., Ito, J., Wu, Z., Nakamura, T., Wahida, A., Doll, S., Tonnus, W., Nepachalovich, P., Eggenhofer, E., Aldrovandi, M., et al. (2022). A non-canonical vitamin K cycle is a potent ferroptosis suppressor. Nature *608*, 778–783. https://doi.org/10.1038/s41586-022-05022-3.

83. Lukow, D.A., Sausville, E.L., Suri, P., Chunduri, N.K., Wieland, A., Leu, J., Smith, J.C., Girish, V., Kumar, A.A., Kendall, J., et al. (2021). Chromosomal instability accelerates the evolution of resistance to anti-cancer therapies. Dev. Cell *56*, 2427–2439.e4. https://doi.org/10.1016/j.devcel.2021.07.009.

84. Stringer, B.W., Day, B.W., D'Souza, R.C.J., Jamieson, P.R., Ensbey, K.S., Bruce, Z.C., Lim, Y.C., Goasdoué, K., Offenhäuser, C., Akgül, S., et al. (2019). A reference collection of patient-derived cell line and xenograft models of proneural, classical and mesenchymal glioblastoma. Sci. Rep. *9*, 4902. https://doi.org/10.1038/s41598-019-41277-z.

85. Sanjana, N.E., Shalem, O., and Zhang, F. (2014). Improved vectors and genome-wide libraries for CRISPR screening. Nat. Methods *11*, 783–784. https://doi.org/10.1038/nmeth.3047.

86. Miyoshi, H., Blömer, U., Takahashi, M., Gage, F.H., and Verma, I.M. (1998). Development of a self-inactivating lentivirus vector. J. Virol. *72*, 8150–8157. https://doi.org/10.1128/jvi.72.10.8150-8157.1998.

87. Czekanska, E.M. (2011). Assessment of cell proliferation with resazurin-based fluorescent dye. Methods Mol. Biol. *740*, 27–32. https://doi.org/10.1007/978-1-61779-108-6_5.

88. Morinaka, A., Funato, Y., Uesugi, K., and Miki, H. (2011). Oligomeric peroxiredoxin-I is an essential intermediate for p53 to activate MST1 kinase and apoptosis. Oncogene *30*, 4208–4218. https://doi.org/10.1038/onc.2011.139.

89. Hashizume, O., Funato, Y., Yamazaki, D., and Miki, H. (2020). Excessive Mg^{2+} Impairs Intestinal Homeostasis by Enhanced Production of Adenosine Triphosphate and Reactive Oxygen Species. Antioxid. Redox Signal. *33*, 20–34. https://doi.org/10.1089/ars.2019.7951.

STAR★METHODS

KEY RESOURCES TABLE

REAGENT or RESOURCE	SOURCE	IDENTIFIER
Antibodies		
Rabbit polyclonal anti-PRL	Funato et al., 2014[14]	N/A
Mouse monoclonal anti-FLAG (clone M2)	Merck	Cat#F1804; RRID: AB_262044
Mouse monoclonal anti-β-actin (clone 2D4H5)	Proteintech	Cat#66009-1-Ig; RRID: AB_2687938
Rabbit monoclonal anti-cleaved caspase-3 (clone 5A1E)	Cell Signaling Technology	Cat#9664; RRID: AB_2070042
Rabbit monoclonal anti-p65 (clone D14E12)	Cell Signaling Technology	Cat#8242; RRID: AB_10859369
Mouse monoclonal anti-PRL3 (clone 318)	Santa Cruz Biotechnology	Cat#sc-130355; RRID: AB_2193531
Rabbit polyclonal anti-IκBα	Cell Signaling Technology	Cat#9242; RRID: AB_331623
Rabbit monoclonal anti-Gasdermin D (GSDMD) (clone E4M2W)	Cell Signaling Technology	Cat#46451; RRID: AB_2921367
Rabbit polyclonal anti-TNFα	Abcam	Cat#ab6671; RRID: AB_305641
Rabbit polyclonal anti-γH2AX	Abcam	Cat#ab11174; RRID: AB_297813
Alkaline phosphatase (AP)-conjugated anti-mouse IgG	Promega	Cat#S3721; RRID: AB_430871
AP-conjugated anti-rabbit IgG	Promega	Cat#S3731; RRID: AB_430872
Horseradish peroxidase (HRP)-conjugated anti-rabbit IgG	Promega	Cat#W4011; RRID: AB_430833
HRP-conjugated anti-mouse IgG	Promega	Cat#W4021; RRID: AB_430834
Alexa Fluor 568-conjugated anti-mouse IgG	Thermo Fisher Scientific	Cat#A-11004; RRID: AB_2534072
Alexa Fluor 568-conjugated anti-rabbit IgG	Thermo Fisher Scientific	Cat#A-11036; RRID: AB_10563566
Alexa Fluor 488-conjugated anti-rabbit IgG	Thermo Fisher Scientific	Cat#A-11008; RRID: AB_143165
Chemicals, peptides, and recombinant proteins		
Z-VAD-FMK	Peptide Laboratory	Cat#3188-v ; CAS: 187389-52-2
liproxstatin-1 (Lip-1)	Sigma	Cat#SML1414; CAS: 950455-15-9
MCC950	TCI	Cat#M3396; CAS: 256373-96-3
VX-765	TCI	Cat#V0176; CAS: 273404-37-8
necrostatin-1 (Nec-1)	StressMarq Biosciences	Cat#SIH-213; CAS: 4311-88-0
KU-55933	Sigma	Cat#SML1109; CAS: 587871-26-9
IMD-0354	Selleck Biotechnology	Cat#S2864; CAS:978-62-1
Human TNFα	PeproTech	Cat#300-01A
Lipopolysaccharide (LPS)	Sigma	Cat#L2630; CAS: 93572-42-0
ATP	Sigma	Cat#A2383; CAS: 34369-07-8
(1S, 3R)-RSL3	Cayman Chemical	Cat#19288; CAS: 1219810-16-8
staurosporine (STS)	FUJIFILM Wako Chemicals	Cat#197–10251; CAS: 62996-74-1
cytochalasin B	FUJIFILM Wako Chemicals	Cat#030–17551; CAS: 14930-96-2
SiR-actin	Cytoskeleton	Cat#CY-SC001
Resazurin	Sigma	Cat# R7017; CAS: 62758-13-8
Critical commercial assays		
Magnesium B-test kit	FUJIFILM Wako Chemicals	Cat#274-83901
Click-iT EdU Imaging Kit	Thermo Fisher Scientific	Cat#C10337
miRNeasy Mini Kit	QIAGEN	Cat#217004
ROS Assay Kit -Photo-oxidation Resistant DCFH-DA-	DOJINDO	Cat#R253

(*Continued on next page*)

Continued

REAGENT or RESOURCE	SOURCE	IDENTIFIER
Deposited data		
Raw RNA-seq data	This study	GEO: GSE309910
Experimental models: cell lines		
HEK293T	Funato et al., 2020[32]	N/A
J774A.1	RIKEN BioResource Research Center	Cat#RCB0434
HT-1080	Mishima et al., 2022[82]	N/A
MDCK	A gift from Dr. Y. Fujita (Kyoto University)	N/A
Oligonucleotides		
Target sequences for CRISPR-Cas9–mediated KO		
Canine *PRL1* sgRNA: 5′-ATTGCTGTCCATTGTGTTGC-3′	This paper	N/A
Canine *PRL2* sgRNA: 5′-TAATGAACCGTCCAGCCCCT-3′	This paper	N/A
Canine *p65* sgRNA: 5′-CCGTCGACAACTCTGAGTTT-3′	This paper	N/A
Primers for amplifying genomic region spanning the sgRNA target site		
PRL1-KO forward: 5′-TCATTCTTTTGATTTAGGATTGGCC-3′	This paper	N/A
PRL1-KO reverse: 5′-GCTGTCCTGGAATACATTATTCTATT-3′	This paper	N/A
PRL2-KO forward: 5′-AGAAAAACACTGATCGATATTAGGCA-3′	This paper	N/A
PRL2-KO reverse: 5′-TGGCTTTGTGATAAGAGATTTCTTT-3′	This paper	N/A
p65-KO forward: 5′- CTGACAGAGGCCCTGCTACAG-3′	This paper	N/A
p65-KO reverse: 5′ ATGTCTGCAATGGAGGAGAAGTCTT-3′	This paper	N/A
siRNAs		
Canine *PRL1*-1: 5′-GCAACTTCTGTATTTGGAGAAGTAT-3′	Sigma	N/A
Canine *PRL1*-2: 5′-CCAACCAAUGCGACCUUAAACAAAU-3′	Sigma	N/A
Control: 5′- AGTTCGATACCGACACTTTCGTCGC-3′	Thermo	Cat#12935200
Recombinant DNA		
pLVX-TetOne-Puro-GFP	Lukow et al., 2021[83]	Addgene plasmid #171123
pLVX-TetOne-CNNM4-FLAG	This paper	N/A
pCMV tag 4A-CNNM4	Yamazaki et al., 2013[4]	N/A
lentiCRISPR v2-hygro	Stringer et al., 2019[84]	Addgene plasmid #98291
lentiCRISPR v2-puro	Sanjana et al., 2014[85]	Addgene plasmid #52961
lentiCRISPR v2-blast	Mohan Babu	Addgene plasmid #83480
pCAG-HIVgp	Miyoshi et al., 1998[86]	RIKEN BioResource Center plasmid #RDB04394
pCMV-VSV-G-RSV-Rev	Miyoshi et al., 1998[86]	RIKEN BioResource Center plasmid #RDB04393
pMD2.G	Didier Trono	Addgene plasmid #12259
psPAX2	Didier Trono	Addgene plasmid #12260
pHyPer-cyto	Evrogen	Cat#FP941

(*Continued on next page*)

Continued

REAGENT or RESOURCE	SOURCE	IDENTIFIER
Software and algorithms		
Prism (version 9.5.1)	GraphPad	http://www.graphpad.com
MetaMorph (version 7.8.4.0)	Molecular Devices	https://www.moleculardevices.com
ImageJ (version 1.54d)	National Institute of Health (NIH)	https://imagej.nih.gov/ij/
FCS express (version 7.24.0024)	*De Novo* Software	https://denovosoftware.com/
Eve (version 1.8.2)	Nanolive	https://www.nanolive.com/products/live-cell-analytics/eve-analytics/
STEVE (version 1.6.3496)	Nanolive	https://www.nanolive.com/microscopy-software/
iDEP (version 0.96)	South Dakota State University	http://bioinformatics.sdstate.edu/idep/
BioJupies	Icahn School of Medicine at Mount Sinai	https://maayanlab.cloud/biojupies/
Enrichr	Icahn School of Medicine at Mount Sinai	https://maayanlab.cloud/Enrichr/

EXPERIMENTAL MODEL AND STUDY PARTICIPANT DETAILS

HEK293T and HT-1080 cells were used as reported previously.[32,82] J774A.1 cells were purchased from RIKEN BioResource Research Center. MDCK cells were gifted by Dr. Yasuyuki Fujita of Kyoto University.

METHOD DETAILS

Cell culture and transient transfection

Cells were cultured in Dulbecco's Modified Eagle medium (DMEM, Shimadzu, 05919, for MDCK, HEK293T, and HT-1080 cells) supplemented with 10% fetal bovine serum (FBS), 50 unit/mL penicillin, and 50 μg/mL streptomycin or in Roswell Park Memorial Institute (RPMI) 1640 medium (Gibco, 31800, for J774A.1 cells) supplemented with 10% FBS, 50 unit/mL penicillin, and 50 μg/mL streptomycin. The expression plasmids were transfected using Lipofectamine 2000 (Thermo Fisher Scientific, 11668019), according to the manufacturer's instructions.

Generation of expression constructs

The complementary DNA (cDNA) of human *CNNM4* was subcloned in a previous study.[4] For transient expression in mammalian cells, *CNNM4* cDNA was inserted into pCMV tag 4A (Agilent Technologies). For DOX-inducible expression in mammalian cells, the GFP-encoding region of pLVX-TetOne-Puro-GFP (gifted by Dr. Jason Sheltzer through Addgene, 171123[83]) was replaced with the *CNNM4* cDNA fused to an N-terminal FLAG tag. The resulting expression construct is hereafter called pLVX-TetOne-CNNM4-FLAG.

Generation of KO cell lines

To establish *PRL1*-, *PRL2*-, or *p65*-KO MDCK cells, sgRNA constructs were generated by inserting oligonucleotides targeting canine *PRL1*, *PRL2*, or *p65* gene into lentiCRISPR v2-hygro (gifted by Brett Stringer through Addgene, 98291[84]), lentiCRISPR v2-puro (gifted by Feng Zhang through Addgene, 52961[85]), or lentiCRISPR v2-blast (gifted by Mohan Babu through Addgene, 83480), respectively. The target sequences are described in the key resources table. Each sgRNA construct was cotransfected with pCAG-HIVgp and pCMV-VSV-G-RSV-Rev (developed by H. Miyoshi of Keio University and provided from RIKEN BioResource Center, RDB04394 and RDB04393, respectively[86]) into HEK293T cells using PEI MAX (Polysciences, 24765). The cell culture supernatant containing the lentiviruses was collected 48 h after transfection, and used to infect MDCK cells (with 6 μg/mL polybrene supplementation, for 48 h). Transduced cells were then selected with the corresponding antibiotics (3–5 μg/mL puromycin, 0.4 mg/mL hygromycin, or 10 μg/mL blasticidin) for 3−7 days, and cell clones were isolated by limiting dilution. For each cell clone, the genomic region spanning the target site was amplified via PCR amplification by using the primers described in the key resources table, ligated into the pMD20 plasmid (Takara, 3270), and analyzed via Sanger sequencing. At least eight independent plasmids were sequenced for each cell clone, and the absence of plasmids containing the wild-type sequence was confirmed.

Transient KD experiments

Duplex siRNAs against canine *PRL1* or the negative control (Thermo Fisher Scientific, 1299003) were transfected twice with Lipofectamine RNAiMAX (Thermo Fisher Scientific, 13778150) at 24 h intervals. The target sequences of each siRNA are described in the key resources table.

Generation of inducible C-terminal FLAG tagged CNNM4 (CNNM4-FLAG)-expressing cell lines

pLVX-TetOne-CNNM4-FLAG was co-transfected with pMD2.G and psPAX2 (gifted by Didier Trono through Addgene, 12259 and 12260, respectively) into HEK293T cells using PEI MAX (Polysciences). Lentivirus-containing supernatants were collected 48 h post-transfection to infect HT-1080 cells (with 10 μg/mL protamine supplementation). Transduced cells were selected with 1 μg/mL puromycin for 48 h, and then single-cell clones were isolated by limiting dilution.

Cell counting

Trypan blue exclusion assays were used to determine the viable cell number and dead cell percentage of MDCK-derived cell lines in a time-course manner. Cells were trypsinized immediately after the second siRNA transfection, and 1.0×10^5 cells were reseeded on 36 mm-dishes and cultured for the period indicated in each figure. In experiments with Mg^{2+} supplementation and *p65*-KO cells, siRNA-transfected cells were used for analyses without reseeding. After collecting the floating cells from the culture supernatants, the attached cells were collected by trypsinization. Solutions containing floating and attached cells were combined and centrifuged at 1,000 rpm for 5 min at 4°C. The cell pellet was resuspended in trypan blue solution, and the number of trypan blue excluded and incorporated cells was counted using a hemocytometer and determined as viable and dead cells, respectively.

Cell viability of HT-1080-derived cell lines were evaluated by resazurin reduction assay (Sigma, R7017).[87] Cells (3.0×10^3) were seeded on 96-well plates with various compounds. After 12 h-incubation, DOX was added to the medium with final concentrations indicated in each figure, and cultured for 48 h. Then, the medium was replaced with a growth medium containing 0.004% resazurin and incubated for 3 h at 37°C. Fluorescence signals were measured at an excitation/emission wavelength of 540/590 nm using the SpectraMax M5 microplate reader (Molecular Devices) or the SH-9000Lab microplate reader (Corona). Cell viability was calculated as follows:

$$\textit{Cell viability ratio}\ (\%) = \frac{\textit{signal of each well} - \textit{background}\ (\textit{signal of well without cells})}{\textit{signal of well with cells without DOX treatment} - \textit{background}} \times 100$$

Quantification of intracellular Mg

For the MDCK-derived cell lines, 8×10^5 cells were seeded on 60-mm dishes, and used 6 h after the second siRNA transfection. For the HT-1080-derived cell lines, 3×10^6 cells were seeded on 100-mm dishes, and used 30 h after the addition of DOX. The cells were washed with PBS and collected by trypsinization. After centrifugation (1,000 rpm, 5 min, 4°C), the cell pellet was resuspended in lysis buffer [50 mM Tris-HCl (pH 8.0), 150 mM NaCl, 1% NP-40, 0.5% sodium deoxycholate, and 0.1% SDS]. For cellular Mg measurement, 6 M HCl was added to the lysates to adjust the pH to 0−2 using a pH test paper and then centrifuged at 15,000 rpm for 10 min at 4°C. The Mg level in the supernatant was quantified using the Mg-sensitive dye xylidyl blue in the Magnesium B-test kit (FUJIFILM Wako Chemicals, 274–83901), according to the manufacturer's instructions. For normalization, protein levels in the lysates (before pH adjustment) were measured using a BCA Protein Assay Kit (Thermo Fisher Scientific, 23225).

Labeling of S-phase cells

Cells in the S-phase were identified using the Click-iT EdU Imaging Kit (Thermo Fisher Scientific, C10337), according to the manufacturer's instructions. Briefly, 1×10^4 cells 6 h after the second siRNA transfection were reseeded on 36-mm dishes containing glass coverslips, and cultured for 48 h. Cells were then incubated with 10 μM EdU for 30 min at 37°C and fixed in 3.7% formaldehyde in PBS for 15 min at room temperature. After permeabilization and blocking with 0.5% Triton X-100 and 3% BSA in PBS for 1 h at room temperature, the incorporated EdU was covalently attached to Alexa Fluor 488 dye via a copper-catalyzed azide-alkyne cycloaddition reaction. Cells were washed three times with PBS and incubated with 1 μg/mL 4′,6-diamidino-2-phenylindole (DAPI, Roche, 10236276001) for DNA staining and then viewed under the confocal scanning laser microscope FLUOVIEW FV1000 (OLYMPUS). Quantification of each image was performed using ImageJ software [version 1.54d, National Institute of Health (NIH)].

Cell cycle analysis

Six hours after the second siRNA transfection, the cells (1.0×10^5) were reseeded on 36-mm dishes and cultured for the period indicated in each figure. After collecting both floating and adherent cells (see Cell counting), the cells were washed with ice-cold PBS and fixed in ice-cold 70% ethanol for 30 min. Fixed cells were washed with PBS and resuspended in staining solution containing 1 μg/mL DAPI and 0.1% Triton X-100 in PBS. The samples were then incubated at room temperature for 30 min in the dark. Fluorescence intensity in each cell was measured (10,000 cells per sample) using a flow cytometer (Attune NxT, Thermo Fisher Scientific). The population of cells in each cell phase was determined by using FCS express software (version 7.24.0024, *De Novo* Software).

Immunofluorescence microscopy

The cells were fixed in PBS containing 3.7% formaldehyde for 15 min at room temperature. After three washes with PBS, the cells were permeabilized and blocked with 0.2% Triton X-100 and 3% FBS in PBS for 1 h at room temperature. The cells were then incubated overnight with the primary antibody in PBS. After three washes with PBS, cells were incubated with the secondary antibody in PBS, and 25 μM rhodamine-conjugated phalloidin (FUJIFILM Wako Chemicals, 165–21641, for F-actin staining) or 1 μg/mL DAPI (for DNA staining) for 30 min at room temperature. After three washes with PBS, the coverslips were mounted on glass slides using a mounting solution [0.5% *o*-phenylenediamine in 20 mM Tris-HCl (pH 8.8), 90% glycerol] and viewed under a confocal scanning laser microscope FLUOVIEW FV1000 or Nikon AX. Quantitative analysis of each image was performed using ImageJ software. The cell number was determined based on the number of nucleic DNA signals. Cells with nuclear p65 localization were defined as cells with a stronger mean nuclear p65 signal intensity per pixel than mean cytoplasmic signal intensity per pixel.

Live cell imaging

For phase-contrast time-lapse imaging, IX81 [OLYMPUS, controlled with MetaMorph software (version 7.8.4.0, Molecular Devices)] or Nikon AX confocal scanning laser microscope were used, which were both equipped with an environmental chamber to maintain a humidified atmosphere of 5% CO_2 at 37°C (Tokai Hit). For MDCK cell lines under PRL suppression, 1×10^4 cells were reseeded on 36-mm glass-based dishes immediately after the second siRNA transfection, and image acquisition was started 3 h after seeding. For HT-1080 cell lines with inducible CNNM4-FLAG expression, 2×10^5 cells were seeded on 36-mm glass-based dishes and treated with 3 μg/mL DOX 12 h after seeding. Image acquisition was initiated 24 h after the DOX treatment. Cytochalasin B was added immediately after the initiation of cell blebbing.

For holotomographic time-lapse imaging, 3D Cell Explorer [Nanolive, controlled with Eve (version 1.8.2) or STEVE (version 1.6.3496) software] was used, which was equipped with an environmental chamber to maintain a humidified atmosphere of 5% CO_2 at 37°C (Okolab). For MDCK cell lines under PRL suppression, 2×10^5 cells after the second siRNA transfection were reseeded on 35-mm μ-Dishes (Ibidi), and image acquisition was initiated 3 h after reseeding. For HT-1080 cell lines with inducible CNNM4-FLAG expression, 2×10^5 cells were seeded on 35-mm μ-Dishes, and treated with 3 μg/mL DOX 12 h after seeding. Image acquisition was initiated 24 h after the DOX treatment. For apoptosis or ferroptosis induction, 2×10^5 cells were seeded on 35-mm μ-Dishes, and image acquisition was started immediately after the addition of 0.3 μM STS or 1 μM RSL3 at 12 h after seeding. Maximum intensity projection images were generated using horizontal section images acquired at 0.5 μm intervals in the z-direction.

For live-cell fluorescence imaging, the Nikon AX confocal scanning laser microscope equipped with an environmental chamber was used to maintain a humidified atmosphere of 5% CO_2 at 37°C (Tokai Hit). For MDCK cell lines under PRL suppression, 2×10^5 cells after the second siRNA transfection were reseeded on 36-mm glass-based dishes, and images were acquired at 3−6 h after reseeding. For HT-1080 cell lines with inducible CNNM4-FLAG expression, 2×10^5 cells were seeded on 36-mm glass-based dishes, treated with 3 μg/mL DOX at 12 h after seeding. Images were acquired at 20−28 h after DOX treatment. For apoptosis induction, 2×10^5 cells were seeded on 36-mm glass-based dishes, treated with 0.3 μM STS at 12 h after seeding, and images were acquired at 4−6 h after STS treatment. To label actin filaments, SiR-actin (Cytoskeleton, CY-SC001; 100 nM for HT-1080 cells and 200 nM for MDCK cells) was added 12 h before image acquisition. For DNA staining, 1 μg/mL Hoechst 33342 (Nacalai tesque, 0491581) was added 10 min before image acquisition. 3D reconstituted images were generated by stacking horizontal section images acquired at 1 μm intervals in the z-direction.

RNA-seq analysis

The cells (3×10^4) were seeded on 36-mm dishes and subjected to siRNA transfection. Eighteen hours after the second transfection, RNA was extracted from the cells using the miRNeasy Mini Kit (QIAGEN, 217004), according to the manufacturer's instructions. Next-generation sequencing (NGS) analysis was performed at the NGS Core Facility of the Research Institute for Microbial Diseases (Osaka University). Data analysis was performed with the following online software: iDEP (version 0.96, http://bioinformatics.sdstate.edu/idep/), BioJupies (https://maayanlab.cloud/biojupies/), and Enrichr (https://maayanlab.cloud/Enrichr/).

Quantification of intracellular H_2O_2 level using HyPer

Intracellular H_2O_2 measurement with ratiometric fluorescent H_2O_2-probe HyPer was performed according to the previous studies.[88,89] Briefly, 1.5×10^5 cells were seeded on 36-mm glass-based dishes, and pHyPer-cyto (evrogen, FP941) was transfected using LipofectAmine2000. 0.1 μg/mL DOX was added 2 h after transfection, and image acquisition was performed 30 h after the DOX treatment with OLYMPUS IX81 microscope. Fluorescence was measured (excitation at 425–445 nm and 470–490 nm; emission at 505–545 nm) using the MetaMorph software. The fluorescence signal intensities of both excitation wavelengths were measured for each cell and the ratio of signal intensity with 470–490 nm excitation to that of 425–445 nm excitation was calculated using MetaMorph.

Measurement of general ROS level using DCFH-DA

General ROS levels in cells were measured using DCFH-DA was performed with ROS Assay Kit -Photo-oxidation Resistant DCFH-DA- (DOIJINDO, R253). Breifly, 3×10^5 cells were seeded on 36 mm dishes, and 0.1 μg/mL DOX was added 12 h after seeding. The cells were trypsinized 30 h later and labeled with DCFH-DA dye for 30 min, and then analyzed by AttuneNxT flow cytometer (Invitrogen). A minimum of 10,000 cells were analyzed in each sample.

QUANTIFICATION AND STATISTICAL ANALYSIS

All statistical data are presented as mean ± standard error of the mean (SEM), and *n* value and what each n represents are described in each figure legend. All *p* values, except for those indicated in Figure 4C and Table S1 were determined using one-way or two-way analysis of variance (ANOVA) using Prism software (version 9.5.1, GraphPad). Holm–Sidak's tests were used for all post hoc tests. *p* values in Figure 4C were determined by Fisher's exact test with Enrichr software. *p* values in Table S1 were determined by Fisher's exact test with Prism software.